Article
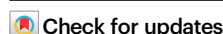
Crystal structures of DCAF1-PROTAC-WDR5 ternary complexes provide insight into DCAF1 substrate specificity

Mark F. Mabanglo[1,8], Brian Wilson[1,8], Mahmoud Noureldin[1,8], Serah W. Kimani [2], Ahmed Mamai[1], Chiara Krausser[1], Héctor González-Álvarez[1,3], Smriti Srivastava[1], Mohammed Mohammed[1], Laurent Hoffer [1], Manuel Chan[1], Jamie Avrumutsoae[1], Alice Shi Ming Li[1,3], Taraneh Hajian[1], Sarah Tucker[1], Stuart Green [2], Magdalena Szewczyk[2], Dalia Barsyte-Lovejoy [2,3], Vijayaratnam Santhakumar [2], Suzanne Ackloo [2], Peter Loppnau[2], Yanjun Li [2], Almagul Seitova[2], Taira Kiyota [1], Jue George Wang[1], Gilbert G. Privé[4], Douglas A. Kuntz [4], Bhashant Patel[5], Vaibhavi Rathod[5], Anand Vala[5], Bhimsen Rout[5], Ahmed Aman [1,6], Gennady Poda[1,6], David Uehling[1], Jailall Ramnauth[1], Levon Halabelian [2,3], Richard Marcellus[1], Rima Al-awar[1,3,7] ✉ & Masoud Vedadi [1,3] ✉

Proteolysis-targeting chimeras (PROTACs) have been explored for the degradation of drug targets for more than two decades. However, only a handful of E3 ligase substrate receptors have been efficiently used. Downregulation and mutation of these receptors would reduce the effectiveness of such PROTACs. We recently developed potent ligands for DCAF1, a substrate receptor of EDVP and CUL4 E3 ligases. Here, we focus on DCAF1 toward the development of PROTACs for WDR5, a drug target in various cancers. We report four DCAF1-based PROTACs with endogenous and exogenous WDR5 degradation effects and high-resolution crystal structures of the ternary complexes of DCAF1-PROTAC-WDR5. The structures reveal detailed insights into the interaction of DCAF1 with various WDR5-PROTACs, indicating a significant role of DCAF1 loops in providing needed surface plasticity, and reflecting the mechanism by which DCAF1 functions as a substrate receptor for E3 ligases with diverse sets of substrates.

The development of small molecule modulators of protein target activities is a widely used strategy in drug discovery[1,2]. However, many cellular targets have been declared undruggable as high-throughput screening, fragment screening, or even structure-activity-relationship (SAR) campaigns failed to identify reliable small molecule binders, partly due to lack of enzymatic activities or suitable small molecule binding sites[3,4]. An alternative approach was taken more than two decades ago to eliminate drug targets through protein degradation[5]. Proteolysis-targeting chimera (PROTAC) for targeted protein degradation for many diverse applications,

[1]Drug Discovery Program, Ontario Institute for Cancer Research, Toronto, ON, Canada. [2]Structural Genomics Consortium, University of Toronto, Toronto, ON, Canada. [3]Department of Pharmacology and Toxicology, University of Toronto, Toronto, ON, Canada. [4]Princess Margaret Cancer Centre, University Health Network, Toronto, ON, Canada. [5]Piramal Discovery Solutions, Pharmaceutical Special Economic Zone, Ahmedabad, Gujarat, India. [6]Leslie Dan Faculty of Pharmacy, University of Toronto, Toronto, ON, Canada. [7]Department of Chemistry, University of Toronto, Toronto, ON, Canada. [8]These authors contributed equally: Mark F. Mabanglo, Brian Wilson, Mahmoud Noureldin. ✉e-mail: ralawar@oicr.on.ca; mvedadi@oicr.on.ca

particularly those in cancer research, has been evolving for many years now[6].

The protein degradation process involves ubiquitin-activating (E1), ubiquitin-conjugating (E2), and ubiquitin ligase (E3) steps. There are more than 600 known E3 ubiquitin ligases with different domain arrangements, mainly the HECT domain containing, RING-finger containing, and RBR types[7]. PROTACs are typically large molecules (~900–1100 Da) with distinct handles that bind to an E3 ligase receptor from one end and the desired drug target destined for degradation from the other end, connected through a linker of sufficient length to bring the two proteins together. Upon ternary complex formation, the targeted protein is polyubiquitinylated, and tagged for degradation via the ubiquitin-26s proteasome system[7]. However, to date, small-molecule ligands have been discovered only for a few E3 ligases, and therefore, the majority of the efforts for many years have been focused on developing Von-Hippel-Lindau (VHL), Cereblon (CRBN), Mouse Doubleminute 2 homolog (MDM2), and Inhibitor of Apoptosis Proteins (IAP)-recruiting PROTACs[8,9]. Out of the 10 reported PROTACs with specified E3 ligase in clinical trials, nine employed CRBN and one used VHL as an E3 ligase[9]. It has been reported that CRBN is mutated or downregulated in resistant tumors to immunomodulatory inhibitory drugs (IMiDs), such as lenalidomide and pomalidomide[10,11]. Such challenges as well as cell or tissue-dependent expression of CRBN and VHL[12] necessitate the need to employ a wider set of validated E3 ligases for targeted protein degradation.

DDB1-CUL4-associated factor 1 (DCAF1) is a substrate receptor for the CUL4 E3 ligase, a RING-type E3. It was originally discovered through binding to the HIV-1 accessory viral protein r (Vpr), and is also called Vpr binding protein (VprBP)[13]. DCAF1 is unique as it also functions as a substrate receptor for a HECT domain containing E3 ligase complex called EDD-DDB1-VprBP (EDVP)[14,15]. Interestingly, the substrates recruited by DCAF1 for these two E3 ligases are nonoverlapping[16]. We recently reported the discovery of OICR-8268, a DCAF1 ligand that binds to its WD40 repeat-containing domain with an SPR K_D of 38 nM, exhibiting cellular target engagement with EC_{50} of 10 μM as measured by cellular thermal shift assay (CETSA)[17]. The discovery of such ligands opens the possibility of DCAF1, an essential protein, becoming a more popular E3 substrate receptor for targeted protein degradation. A DCAF1-directed electrophilic PROTAC (YT47R) was discovered through a chemical proteomic approach, which is reacting with a ligandable cysteine (C1113) and promotes exogenous FKBP12 degradation in a stereo- and site-selective manner[18]. A reversible DCAF1-BRD9 PROTAC (DBr-1) has also been reported along with validation of specific degradation through CRL4 ^{DCAF1} E3 ligase[10,19]. The chemical structures of these PROTACs are presented in Supplementary Fig. 1[10,19].

WDR5 is a WD40 repeat-containing protein that is essential for the regulation of multiple cellular processes[20]. It has been extensively studied as a component of mixed lineage leukemia protein complexes that catalyze histone H3 lysine 4 (H3K4) di- and tri-methylation, and is a validated cancer target (reviewed in[21]). A number of small molecule antagonists of its interaction with MLL have been previously reported[22–24]. MM-401, a macrocyclic peptidomimetic, binds to the Win site of WDR5 (K_D value of about 1 nM) by mimicking the arginine of the Win motif and inhibits the methyltransferase activity of MLL1 complexes in vitro[24]. Small molecule antagonists of WDR5 interactions[22,23,25–28] including OICR-9429, which binds to WDR5 with a K_D of 93 ± 28 nM have also been reported[22]. The oncogenic p30 isoform of C/EBPα binds better to WDR5 and WDR5-containing complexes than non-oncogenic isoforms and the effect of OICR-9429 on AML cells that carry the p30 isoform of the transcription factor C/EBPα further supported the WDR5 role[22]. Follow-up reports also indicated that cells expressing gain-of-function (oncogenic) p53 mutants which comprise the largest group of TP53 mutations in human cancer are uniquely sensitive to OICR-9429[29]. In another report, OICR-9429 reduced N-Myc/WDR5 complex formation, N-Myc target gene expression, and cell growth in neuroblastoma cells[30].

Here, we report on the development of various DCAF1-WDR5 PROTACs that degrade exogenous and endogenous WDR5. These PROTACs not only constitute an alternative potential approach for the development of WDR5-targeted cancer therapeutics but also confirm that DCAF1 could be a suitable ligase receptor to add to the current repertoire of ligase receptors such as CRBN and VHL. We also present four high-resolution crystal structures of DCAF1-PROTAC-WDR5 ternary complexes, providing new structural insights into the interaction of DCAF1 with WDR5-PROTAC pairs and highlighting the significance of DCAF1 loop plasticity in substrate selection and presentation to the E3 ligase.

Results
### PROTAC development and characterization

Recently we reported the development of potent and selective DCAF1 WDR domain binders[17]. Leveraging our extensive contribution to the development of potent, selective, and cell active WDR5 ligands[22,23,25,29,31], we set out to investigate the viability of DCAF1 ligands as handles for WDR5 degradation. The disclosure of VHL[32,33] and CRBN[34] recruiting degraders of WDR5 further encouraged us to pursue the development of a DCAF1-based WDR5 degrader strategy. Based on the crystal structure of OICR-8268 as our starting point (PDB ID: 8F8E)[17], we modified the core pyrazole to allow for a substitution that would proceed along a vector to access the exposed solvent front (Fig. 1a). Unfortunately, the direct substitution on the pyrazole core abolished the DCAF1 potency, as previously discussed[17]. However, switching from pyrazole to pyrrole allowed for such substitution while maintaining activity for DCAF1 (Fig. 1b).

In order to pursue the design strategy, we opted to start with the WDR5 binders that we had previously developed and were used within the VHL-based PROTAC[33]. To link the two components of the PROTACs together, we started with simple alkyl and PEG-based systems to vary the length from 2 to 14 atoms to confirm if recruiting DCAF1 could lead to WDR5 degradation (Fig. 1c).

We initially discovered that only the longest PEG-based linker-containing PROTAC **1** (OICR-40333) and PROTAC **2** (OICR-40407) (Fig. 2) of the first cohort formed DCAF1-PROTAC-WDR5 ternary complexes (Fig. 3a, b) and were able to degrade exogenous (Fig. 3d, e) and endogenous (Fig. 3g, h) WDR5. Therefore, we dismissed all other bifunctional molecules we synthesized up to that point despite binding to each of WDR5 and DCAF1 separately. Following this trend, we made additional PROTACs with even longer PEG-based linkers (Fig. 2).

PROTAC characterization

The PROTAC **1, 2**, and **3** were orthogonally tested by differential scanning fluorimetry (DSF) assay as described in Methods[35], to assess their binding to DCAF1 and WDR5 alone, and to both proteins together as a ternary complex (Supplementary Fig. 2). In DSF, binding of a small molecule to the protein stabilizes the target and leads to an increase in melting temperature (T_m). In this experiment, all three PROTACs (**1-3**) stabilized both WDR5 and DCAF1 proteins, a confirmation of binding of these PROTACs to both proteins. Notably, the stabilization of WDR5 was more pronounced than that of DCAF1 (Supplementary Fig. 2a, b, d). PROTAC **1** and PROTAC **2** showed similar patterns and levels of stabilization of DCAF1 (ΔT_m of 7.5 ± 0.1 °C and 8.0 ± 0.1 °C, respectively) and WDR5 (ΔT_m of 10.6 ± 0.1 °C and 13.4 ± 0.1 °C, respectively). Interestingly, PROTAC **3** with the longest linker among the three PROTACs, showed less stabilization of both DCAF1 (ΔT_m of 5.3 ± 0.1 °C) and WDR5 (ΔT_m of 5.9 ± 0.1 °C). To test ternary complex formation, we also elected to employ DSF. It has previously been reported that binding of small molecules to different domains of a protein will have differential stabilization effects on domain melting[36]. Therefore, a
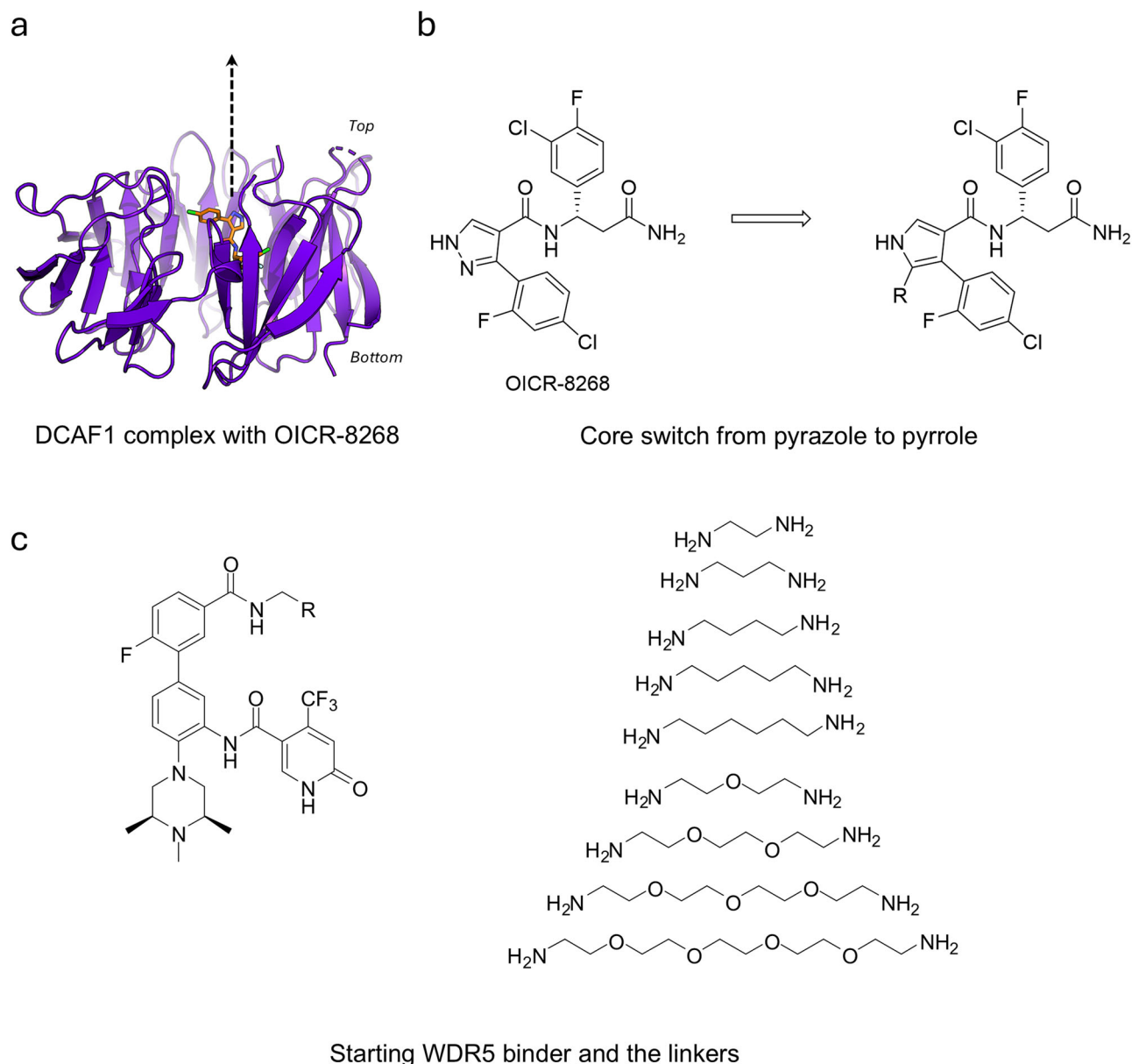
Fig. 1 | Design and chemical synthesis of DCAF1-based PROTACs. a Crystal structure of DCAF1 in complex with OICR-8268 (PDB 8F8E). PROTAC design extends from the pyraz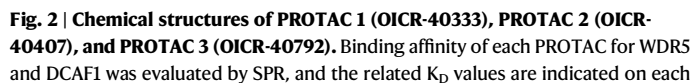ole group of OICR-8268 close to the top side of DCAF1 into the solvent space. **b** The pyrazole group of the DCAF1 anchor was changed to pyrrole to facilitate PROTAC synthesis without loss of activity. **c** The WDR5 anchor (left) was connected to the DCAF1 anchor through various potential linkers (right).

mixture of proteins in solution is expected to behave in a similar manner. The melting curves of DCAF1 and WDR5 together in solution show double peaks representing the melting of DCAF1 first, followed by WDR5 denaturation (Supplementary Fig. 2c). In the presence of the PROTACs, the DCAF1-WDR5 melting curves changed shape and/or shifted slightly rightward, supporting ternary complex formation (Supplementary Fig. 2c).

Binding affinity of all three PROTACs to DCAF1 and WDR5 was also confirmed by SPR with double-digit nanomolar K_D values and reasonable residence times as expected (Supplementary Fig. 3a–c). SPR was also employed to assess the ternary complex formation (Fig. 2a, b, c). Although some background nonspecific binding for WDR5 was observed, a significant increase in R_{max} (SPR maximum response unit) values for PROTAC **1-3** binding to DCAF1 in the presence of WDR5 (0.25 μM) was a clear indication of DCAF1-PROTAC-WDR5 ternary complex formation (Table 1). This increase was more pronounced for PROTAC **3** than PROTAC **1** and PROTAC **2** (**3** > **2** > **1**).

Interestingly, the K_D values of all three PROTACs for binding to DCAF1 were also significantly decreased and the observed residence time ($1/k_{off}$) increased in the presence of WDR5, indicating some level of cooperativity (Table 1). Overall, binding of PROTAC **1-3** to WDR5 increased their affinities for DCAF1, resulting in a more stable ternary complex.

The ability of PROTACs **1-3** to engage DCAF1 and WDR5 in the cell and enable the degradation of exogenous and endogenous WDR5 was evaluated. In exogenous HiBiT WDR5 degradation assay, MV4-11 cells expressing HiBiT-tagged WDR5 (Hb-WDR5) were used to test PROTACs at 12 different concentrations ranging from 2 nM to 10 μM (Fig. 3d-f). PROTAC **1, 2**, and **3** degraded HiBiT-WDR5 with EC_{50} values of 288 ± 137 nM (D_{max} of 31.6 ± 5.5 %), 200 ± 28 nM (D_{max} of 41.2 ± 2.5 %), and 54 ± 18 nM (D_{max} of $41.9 \pm 4.5\%$), respectively. Although full degradation of exogenous WDR5 was not achieved by PROTAC **1-3**, it appears that increases in linker length may have a positive effect within the given range. The effects of PROTAC **1-3** at

Fig. 2 | Chemical structures of PROTAC 1 (OICR-40333), PROTAC 2 (OICR-40407), and PROTAC 3 (OICR-40792). Binding affinity of each PROTAC for WDR5 and DCAF1 was evaluated by SPR, and the related K_D values are indicated on each structure as mean ± SD. SPR experiments were performed in triplicate. Source data are provided as a Source Data file.

the same concentration range (2 nM to 10 μM) on endogenous WDR5 degradation were also assessed using parental MV4-11 cells. PROTACs **1**, **2**, and **3** degraded endogenous WDR5 with EC_{50} values of 186 ± 89 nM (D_{max} of 23.5 ± 11.4%), 135 ± 6 nM (D_{max} of 21.9 ± 11.1%) and 93 ± 37 nM (D_{max} of 33.4 ± 6.8%), respectively (Fig. 3g–i). All three PROTACs showed some hook effect at concentrations above 1 μM,

which in part may explain the lack of complete degradation. None of the PROTACs showed any toxicity within the tested concentration range (Supplementary Fig. 4). The trend of the decrease in endogenous and exogenous degradation EC_{50} values for PROTAC **1** to PROTAC **3** indicates a positive correlation with the increase in SPR complex residence time for these PROTACs.
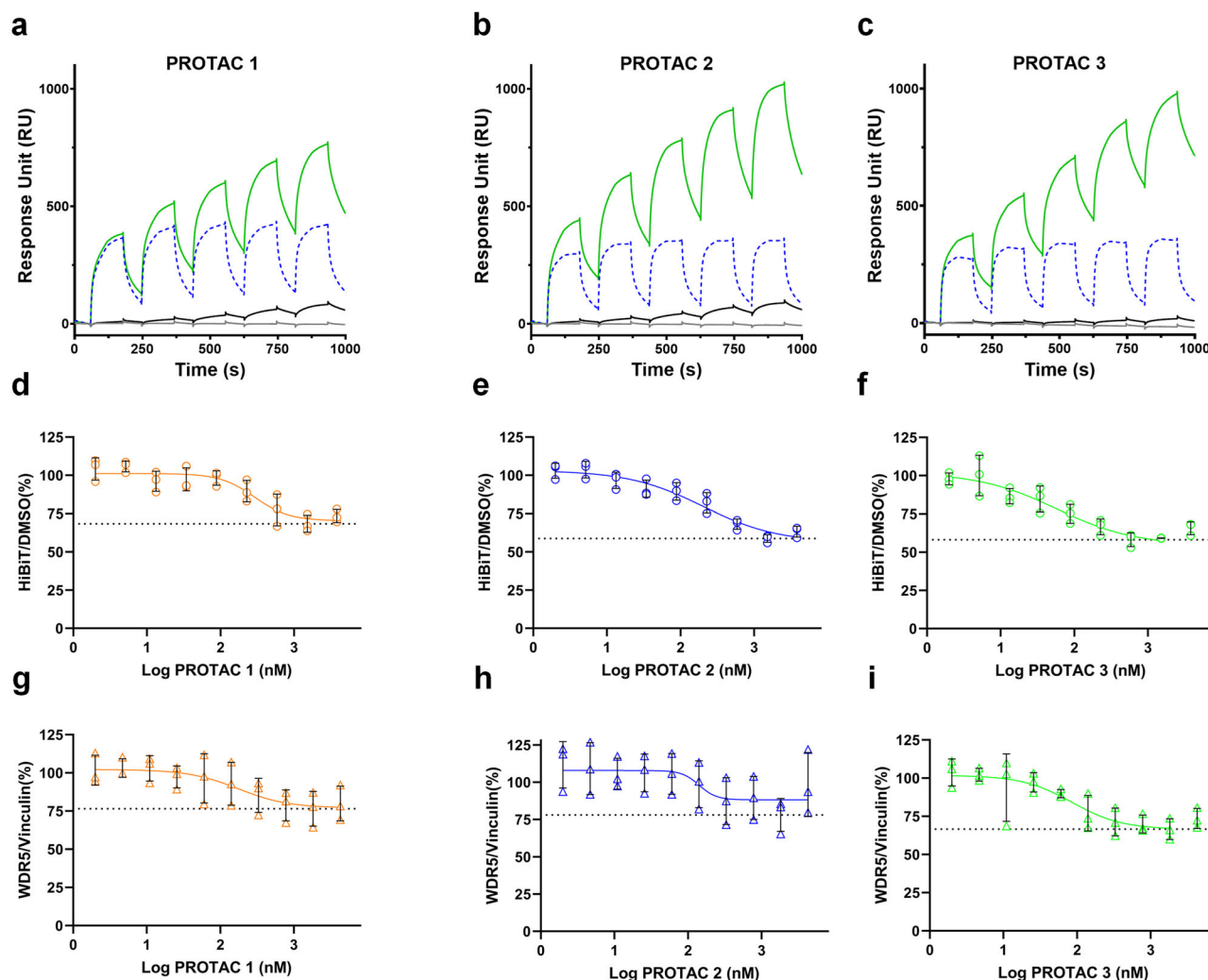
Fig. 3 | Ternary complex formation and WDR5 degradation effect of PROTAC 1-3. a–c DCAF1-PROTAC-WDR5 ternary complex formation of (**a**) PROTAC **1**, (**b**) PROTAC **2**, and (**c**) PROTAC **3** were evaluated by SPR. Biotinylated DCAF1 was immobilized on a high-affinity streptavidin chip. A blank injection was used as a baseline (gray lines). Each PROTAC alone was tested for binding to DCAF1 (black lines). WDR5 at 0.25 μM was injected independently over the flow cells with the immobilized DCAF1 as a reference (blue dash lines). Solutions with ratio of 1 (PROTAC):10 (WDR5; fixed final concentration of 0.25 μM) were injected for ternary complex formation (green line). Although some background nonspecific binding for WDR5 was observed, in the presence of all three PROTACs a significant increase in RU (response unit) was observed indicating DCAF1-PROTAC-WDR5 ternary complex formation. The effect of PROTAC 1–3 treatment of MV4-11 cells on (**d–f**) exogenous and (**g–i**) endogenous WDR5 degradation was assessed. The amount of WDR5 was quantified using the exogenous (HiBiT) and endogenous (ProteinSimple's Jess) WDR5 degradation assays as described in Methods. Results are shown as average ± SD of biological replicates (*n* = 3). Source data are provided as a Source Data file.

Structures of PROTAC ternary complexes show different orientations of WDR5 relative to DCAF1

To further confirm ternary complex formation and better understand the impact of linkers in both enabling the DCAF1-WDR5 interaction and positioning WDR5 for DCAF1-mediated degradation, we solved the crystal structures of DCAF1-PROTAC (**1-3**)-WDR5 ternary complexes. Using heterologously expressed and purified proteins, we solved by molecular replacement the high-resolution crystal structures of DCAF1 and WDR5 in ternary complexes with PROTAC **1**, **2**, and **3** using previously determined structures of the WDR domains of DCAF1 (PDB id 8F8E) and WDR5 (PDB id 2GNQ) as search models (Fig. 4a)[17,37]. The structures were refined to a resolution of 1.92–2.06 Å with an R-work/R-free of 0.1719–0.2108/0.1830–0.2291, with greater than 99.5% of residues in favored and allowed Ramachandran regions (Supplementary Table 1). Importantly, electron density for the PROTAC was seen in a simulated annealing composite omit map for each ternary complex (Supplementary Fig. 5a–c). Iterative structure refinement resulted in a clear $2F_o$-F_c electron density map that allowed mapping of all atoms for each PROTAC and their interactions in ternary complex with DCAF1 and WDR5 (Fig. 4a, Supplementary Fig. 5d–f).

Both DCAF1 and WDR5 have a β-propeller domain topology consisting of seven blades, each formed by four antiparallel β-strands interconnected by loops of varying lengths (Supplementary Fig. 6). In each of these proteins, the first N-terminal β-strand is part of the seventh blade and connects to the first β-strand of the first blade. Since the PROTACs were built using DCAF1 and WDR5 anchors that bind to the top pocket of the protein's WDR domains, as expected the ternary complexes show each PROTAC connecting the two proteins in a top-to-top orientation (Fig. 4a). In the PROTAC **1** ternary complex, WDR5 sits on top of DCAF1 in a tilted orientation due to bending of the WDR5 anchor relative to the straight, extended configuration of the rest of PROTAC **1**. Interestingly, the PROTAC **2** and PROTAC **3** ternary complex structures show protein arrangements in which DCAF1 and WDR5 are in essentially the same orientation with respect to each other and superimpose with an r.m.s.d. of 0.20 Å. In both complexes, the longer PROTAC linkers turn inside the protein interface in a screw-like

Table 1 | Assessment of ternary complex formation by SPR

Sample	K_D (nM)	k_{on} (1/Ms)	± STDEV	k_{off} (1/s)	±STDEV	R_{max}
PROTAC **1**	46 ± 0.4	2.49 E + 05	2.24 E + 04	0.011	9.00 E-04	101
WDR5 + PROTAC **1**	18 ± 1.6	1.52 E + 05	4.94 E + 03	0.003	3.00 E-04	390
PROTAC **2**	38 ± 0.6	2.05 E + 0.5	1.10 E + 05	0.008	4.10 E-03	106
WDR5 + PROTAC **2**	10 ± 0.5	2.04 E + 05	1.60 E + 04	0.002	2.00 E-04	621
PROTAC **3**	48 ± 2.8	6.96 E + 04	1.54 E + 03	0.003	1.00 E-04	42
WDR5 + PROTAC **3**	13 ± 0.5	1.08 E + 05	6.49 E + 03	0.001	7.38 E-05	685
PROTAC **4**	59 ± 0.9	2.39 E + 05	1.03 E + 04	0.014	8.00 E-04	102
WDR5 + PROTAC **4**	5 ± 0.4	1.38 E + 05	2.10 E + 04	0.001	9.41 E-05	818

DCAF1 was immobilized, and binding of PROTACs in the presence and absence of WDR5 was evaluated. The experiments were performed in triplicate. Values are from Fig. 3a–c and Fig. 6b. Source data are provided as a Source Data file.

fashion, resulting in a placement of the WDR5 protein where its 7-fold pseudosymmetry axis is more aligned to that of DCAF1 than in the PROTAC **1** ternary complex (Fig. 4a).

DCAF1 and WDR5 anchors of PROTACs are stabilized by various noncovalent interactions

Similar to the binding of OICR-8268 to DCAF1[17], the shared DCAF1 anchor of PROTAC **1-3** is stabilized in the protein pocket by hydrogen bonds (H-bonds), electrostatic, hydrophobic, and van der Waals interactions with protein residues (Fig. 4b, Supplementary Fig. 5d–f). Briefly, an H-bond/electrostatic interaction occurs between a carbonyl group of the DCAF1 anchor and the guanidinium group of R1298 (blade 6). Together with R1225 (loop connecting blades 3 and 4, i.e. 3–4 loop), R1298 forms an "arginine clamp" that forms a cation-π interaction with the 2,4 di-halogenated aromatic ring of the DCAF1 anchor. Further stabilizing the DCAF1 anchor in the pocket are two H-bonds between its pyrrole group and the peptide carbonyl groups of T1097 (blade 1, water-mediated) and F1355 (blade 7, direct), and its backbone amino group and the carboxylate group of D1356 (blade 7). Another amino group forms H-bonds with the side chain carboxylate group of D1356 and the peptide carbonyl group of C1099 (blade 1, water-mediated). A carbonyl group of the DCAF1 anchor participates in an H-bond with the imidazole group of H1140 (blade 2). Several hydrophobic side chains line the pocket and form stabilizing interactions with the aromatic rings of the DCAF1 anchor. These interactions contribute to the tight binding of the PROTAC to DCAF1 (Figs. 3, 4b, and Supplementary Figs. 3, 5d–f).

Contraposed to the DCAF1 anchor, the WDR5 anchor on the other end of each PROTAC binds the WDR5 pocket predominantly through hydrophobic interactions using two substituted heterocyclic rings and two substituted phenyl rings (Fig. 4c, Supplementary Fig. 5d–f). Two water molecules bridge an H-bond between a carbonyl group of the WDR5 anchor and the peptide amino group of C261 (5-6 loop), and an N atom of the piperazine ring of the WDR5 anchor and the peptide carbonyl group of C261. The piperazine ring is found in a stable chair conformation inside the binding pocket. Finally, two amino groups of the WDR5 anchor participate in H-bonding with the side chain hydroxyl group of S91 (blade 2) and carboxylate group of D107 (blade 2) while the latter interaction is not possible with the corresponding benzene ring of PROTAC **3** (Figs. 2, 4c). PROTAC-induced proximity also enables DCAF1 to form part of the WDR5 anchor binding pocket using the indole group of W1156 (blade 2) (Fig. 4c, Supplementary Fig. 5e, f).

### The DCAF1-WDR5 interface changes with increasing PROTAC linker length

The surface representations in Fig. 5a show different overall shapes of the PROTAC ternary complexes. These differences are due to the changing juxtaposition of WDR5 and DCAF1 in the complexes, arising from the rotation of the WDR5 anchor relative to the DCAF1 anchor.

Superposition of the DCAF1 component of the three complexes shows that WDR5 in both PROTAC **2** and PROTAC **3** ternary complexes is tilted vertically by 8° and rotated clockwise by 152° from its position in the PROTAC **1** complex (Supplementary Fig. 7). The ternary complexes also exhibit diminishing contacts between DCAF1 and WDR5 with increasing linker length of the bound PROTAC, despite the PROTACs having similar effective lengths inside the complex (Fig. 5a). This arises from the changing blade interactions engendered by WDR5 tilting and rotation relative to DCAF1 (Fig. 5b–d, Supplementary Fig. 7). Among the three, the PROTAC **1** ternary complex has the largest buried surface area[38] at the protein interface (1100 Å²), which is stabilized by H-bonding and electrostatic interactions between DCAF1 and WDR5 loop residues. Briefly, these H-bond/electrostatic interactions occur between the side chains of N1132 (DCAF1 blade 1) and K67 (WDR5 blade 1), the side chain of N1135 (1–2 loop) and the peptide carbonyl of A65 (WDR5 blade 1), the side chains of E1091 (DCAF1 blade 7-1 loop) and K87 (WDR5 blade 1–2 loop), the side chain of K1327 (DCAF1 blade 6) and the peptide bond carbonyl of S129 (WDR5, blade 2–3 loop), and the side chains of R1325 (DCAF1 blade 6) and E151 (WDR5 blade 3) (Fig. 5b). DCAF1's R1325 and K1327 residues are found in the protein's longest loop of blade 6 spanning residues 1313–1333 (Supplementary Fig. 6). This flexible loop is fully resolved in the PROTAC **1** ternary complex but not in the PROTAC **2** and **3** ternary complexes, and its conformation varies from one complex to another.

In the PROTAC **2** ternary complex, the protein interaction's buried surface area is decreased (820 Å²), with DCAF1 and WDR5 brought together by PROTAC **2** and further held together by three electrostatic/H-bonding interactions involving the side chain of R1325 (DCAF1 blade 6) and the side chains of Y260 (WDR5, blade 5–6 loop) and D302 (WDR5, blade 6–7 loop) (Fig. 5a, c). In the PROTAC **3** ternary complex, H-bonding and electrostatic interactions are absent, and only three pairs of amino acid residues are close enough to each other to participate in hydrophobic and van der Waals interactions. These pairs of opposing residues include Q1158 (DCAF1 blade 2) and E151(WDR5 blade 3), W1156 (DCAF1 blade 2) and Y191 (WDR5 blade 4), and L1378 (DCAF1 blade 7) and N323 (WDR5 blade 7) (Fig. 5d). Like DCAF1's R1325 and K1327 residues that comprise blade 6's long flexible loop involved in WDR5 binding, the L1378 residue is part of a nearby flexible loop in blade 7, spanning residues 1372–1381, that has different conformations across the ternary complexes (Fig. 5b–d). These flexible loops appear to be important in binding each WDR5-PROTAC pair to form the ternary complex. Nevertheless, the paucity of stabilizing non-covalent forces at the DCAF1-WDR5 interface highlights the dominant role of the PROTACs in bringing the two proteins together to form the ternary complex.

PROTAC linkers assume similar effective lengths in ternary complexes

The similar effective lengths of PROTACs in the ternary complexes, measured as the distance between the para fluorine atom of the
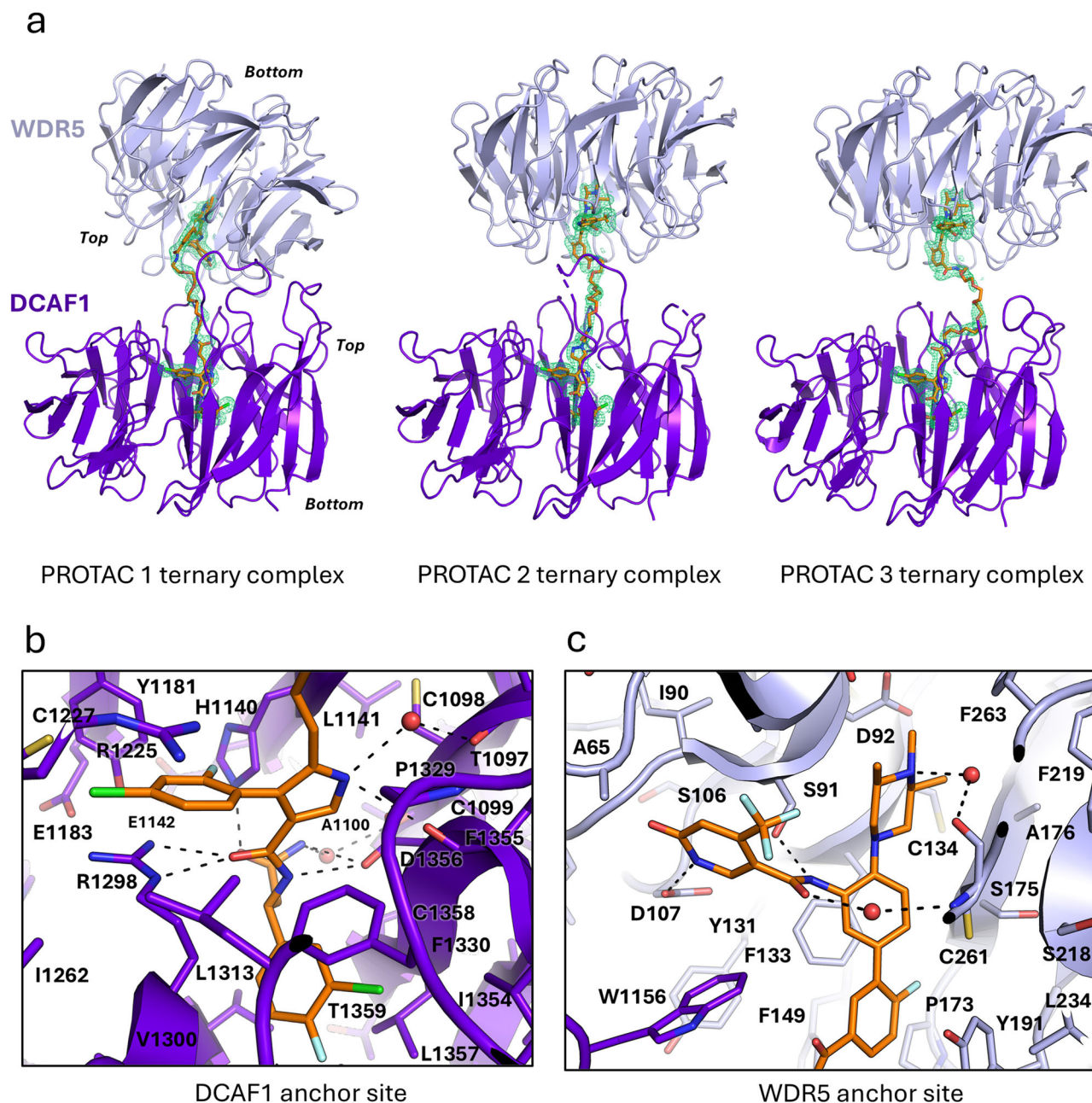
Fig. 4 | Crystal structures of ternary complexes of DCAF1 and WDR5 with PROTACs. a Cartoon representation of ternary complexes showing the top-to-top orientation of the WDR domains of DCAF1 (purple) and WDR5 (light blue). PROTAC **1**, **2**, and **3** are depicted in orange sticks. A $2F_o\text{-}F_c$ electron density map surrounds each PROTAC. **b, c** The DCAF1 and WDR5 anchors of PROTAC **1-3** are stabilized in their respective binding sites by various electrostatic and hydrogen bonding interactions, in addition to surrounding hydrophobic and van der Waals interactions, with protein side chains (sticks). Some hydrogen bonds between PROTAC and DCAF1/WDR5 residues are mediated by water molecules (red spheres). Hydrogen/electrostatic bonds are shown as broken black lines.

DCAF1 anchor and the N-methyl carbon atom of the WDR5 anchor, was an unexpected finding (Fig. 5a). In the PROTAC **1** ternary complex, this length is 39.1 Å for the extended form of PROTAC **1**. In contrast, in the ternary complexes, PROTAC **2** and **3** have an effective length of 38.2 Å, despite having longer linkers than PRO-TAC **1**. To fit inside the binding space between DCAF1 and WDR5, the linkers of PROTAC **2** and **3** compact by making a turn beginning at C5 of the pyrrole ring of the DCAF1 anchor. The PROTAC **3** linker makes a wider turn and has a smaller pitch than that of PROTAC **2** to fit inside the binding pocket (Supplementary Fig. 8). Their linkers then merge at the carbonyl carbon of the WDR5 anchor, arriving at the same position for their WDR5 anchors that is yet distinct to that in the PROTAC **1** ternary complex. Overall, this leads to two different orientations for WDR5 in the ternary complexes (Supplementary Fig. 7, 8).

PROTAC linker curving engenders different interaction patterns at the DCAF1-WDR5 interface

Different interaction patterns involving protein residues and ordered water molecules help in stabilizing PROTAC linker configurations observed in crystal structures (Fig. 5e–g). In the PROTAC **1** ternary complex, the extended linker is stabilized by various hydrophobic and van der Waals interactions with protein residues lining the pocket, mainly from nearby β-strands and loops of blades 1 and 2 (Fig. 5e). The imidazole group of W1156 (blade 2) of DCAF1 forms water-bridged H bonds with an amide carbonyl group proximal to the WDR5 anchor,
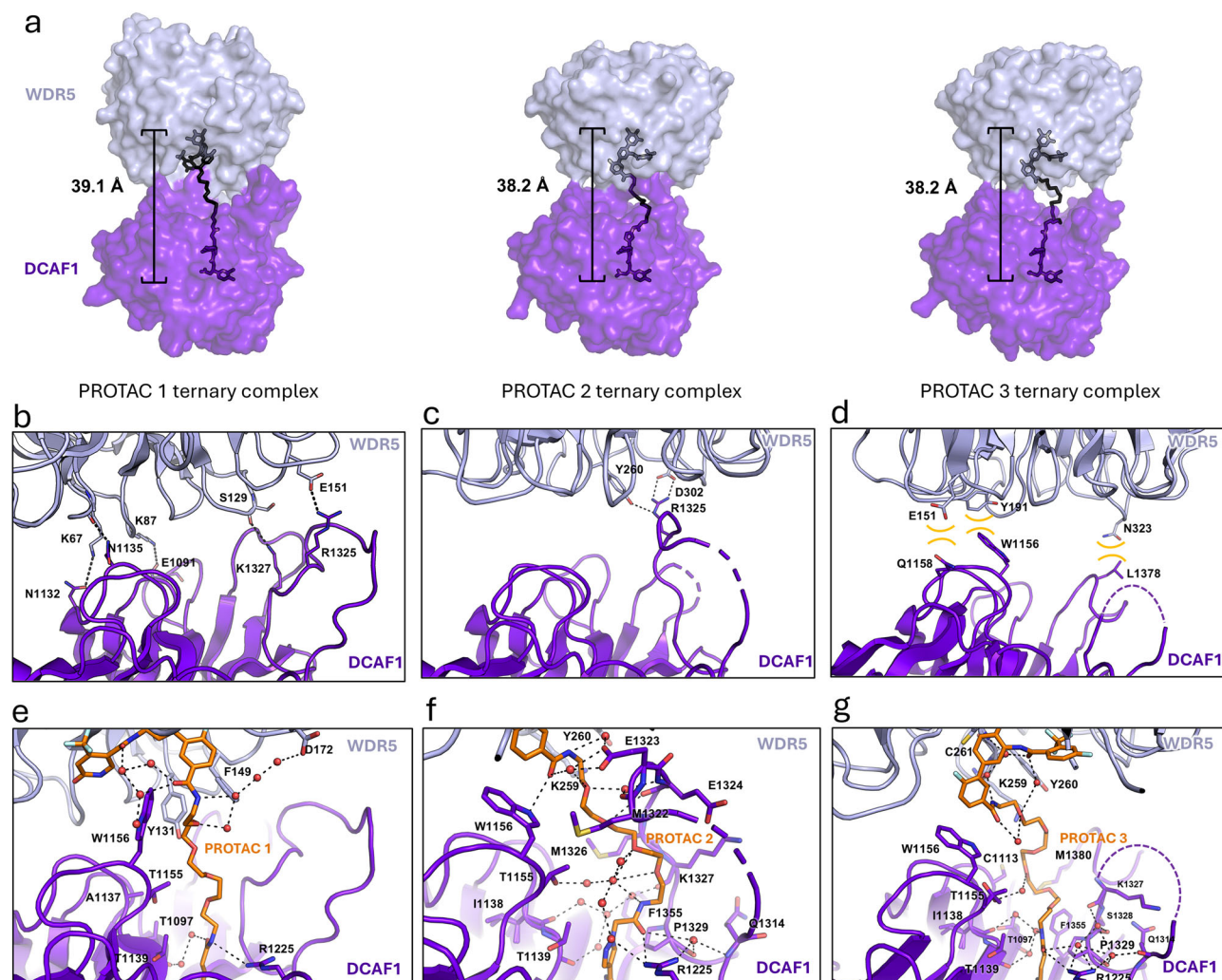
Fig. 5 | Structural details of the DCAF1-WDR5-PROTAC interactions and their significance to PROTAC activity. a PROTAC **1-3** bring DCAF1 and WDR5 together to form a ternary complex. The longer PROTAC **2** and **3** are compressed to a similar effective length as PROTAC **1** in the ternary structures. Surface representations also indicate diminishing contacts between WDR domains with increasing PROTAC linker length. DCAF1 and WDR5 are colored as in Fig. 4. **b–d** Interactions between the top side of the WDR domains of DCAF1 and WDR5 in ternary complex with PROTAC change depending on linker length. Hydrogen bonding and electrostatic interactions are shown as broken black lines. Hydrophobic/van der Waals interactions are shown as brown concave lines. In the presence of PROTAC **1** or **2**, the DCAF1-WDR5 interaction is mediated by various hydrogen bonds (**b**, **c**), which disappear in the interface as the linker becomes longer. Weak hydrophobic/van der Waals interactions sustain the DCAF1-WDR5 interface in the presence of the longest PROTAC **3** (**d**). **e–g** PROTAC linkers of different lengths are accommodated inside the space formed by DCAF1 and WDR5 by compacting. **e** PROTAC **1** (orange sticks) assumes a fully extended configuration inside the pocket. A flexible loop, formed by DCAF1 residues 1313-1333, is retracted away from the PROTAC linker, resulting in an open cavity filled with water molecules. Only water molecules participating in hydrogen bonding with nearby solvent and/or protein residues are shown. **f** The longer PROTAC **2** linker is kinked inside the DCAF1-WDR5 interface. Notably, the flexible loop formed by DCAF1 residues 1313−1333 assumes a different configuration that cradles the curved portion of the linker. In addition, a rotamer shift for DCAF1's W1156 occurs to complement linker shape. **g** The compacted linker of PROTAC **3**, longer than those of PROTAC **1** and **2**, engenders a new interaction pattern with protein residues. The longer linker is further compressed inside the binding space, resulting in a more curved configuration. The nearby loop of DCAF1 (residues 1313–1333, with residues 1315−1326 disordered and not modeled) is displaced from its original location in the PROTAC **1** and **2** ternary complexes.

while also providing a hydrophobic binding face for the aliphatic parts of the linker as it is wedged in between the linker and three aromatic rings. In addition, DCAF1 residue T1097 (blade 1) uses a peptide carbonyl group to form water-mediated H-bonds with the amide carbonyl proximal to the DCAF1 anchor, while R1225 (3–4 loop) forms a direct H-bond with the amide N-H of the linker. The DCAF1, blade 6 flexible loop (residues 1313–1333) is fully ordered but does not interact with the PROTAC 1 linker, leaving a solvent-filled cavity. However, through the R1325 (DCAF1)-E151 (WDR5) salt bridge, the flexible DCAF1 loop extends towards the surface of WDR5, thereby forming a significant part of the wall of the linker's binding pocket (Fig. 5b, e). In WDR5, D172 (3–4 loop) forms water-mediated H-bonds with the amide N-H group and the oxygen atom of the PEG subunit proximal to the WDR5 anchor.

In the PROTAC 2 ternary complex, the PROTAC linker is curved and stabilized predominantly by H-bonds with DCAF1 residues, most of which are mediated by water molecules (Fig. 5f). Importantly, the blade 6 flexible loop (residues 1313–1333) assumes a different, "close lid" conformation whose shape complements the curvature of the linker. Although residues 1317–1320 of this loop could not be modeled, the conformation of the rest of the loop could be confidently assigned and is seen to form important interactions with the PROTAC 2 linker. For instance, the side chains of M1322 and M1326 straddle the linker, forming a "methionine clamp" around the midsection. The peptide backbone groups of E1324, K1327, and M1332 form water-mediated H-bonds with the linker, while E1323 uses its side chain carboxylate group to form water-mediated H-bonds. The missing residues 1317–1320 of

the flexible loop (DEDD sequence), although not modeled due to disorder, likely interact with both polar and nonpolar atoms of the linker through their side chains. Other solvent-bridged H-bonds with the linker involve the peptide carbonyl groups of I1138 and T1139 (blade 2), and the side chain hydroxyl group of T1155 (blade 2). The indole group of W1156 (blade 2) participates in a direct H-bond with the amide carbonyl proximal to the WDR5 anchor. The guanidinium group of R1225 (blade 3–4 loop) also forms both direct and water-mediated H-bonds with the linker, while at the same time helping maintain loop conformation through water-mediated H-bonds with the peptide amino group of Q1314 (blade 6) and the peptide carbonyl group of P1329 (blade 6). An extensive network of hydrophobic and van der Waals interactions exists inside the binding pocket between the PROTAC **2** linker and DCAF1 residues, whose side chains collectively determine the overall shape of the pocket. Notably, the indole group of W1156 (blade 2) undergoes a rotation from that seen in the PROTAC **1** ternary complex, presumably to adjust to the shape of and form a better binding pocket for the linker. Finally, even though no WDR5 residue interacts with the PROTAC **2** linker via H bond, the side chains of WDR5 residues K259 (blade 5–6 loop) and Y260 (blade 5–6 loop) form a binding surface for a portion of the linker.

The structure of the PROTAC **3** ternary complex reveals a more compressed PROTAC **3** linker constrained by the available space between DCAF1 and WDR5 (Fig. 5g, Supplementary Fig. 8). This configuration is sustained by several H-bond interactions with DCAF1 residues, most of which are bridged by water molecules. Interestingly, this configuration is stabilized by water-mediated H-bonds between polar atoms of PROTAC **3** itself. As in the PROTAC **2** ternary complex, W1156 (blade 2) of DCAF1 provides a hydrophobic face to bind the WDR5 anchor and part of the linker that follows, yet is no longer wedged between the linker and aromatic rings as seen in the PROTAC **1** complex due to rotation of the WDR5 anchor (Fig. 5e, g). A direct H-bond with the amide carbonyl group of the linker near the DCAF1 anchor occurs using the guanidinium group of R1225 (blade 3–4 loop), which, like in the PROTAC **2** ternary complex, helps position the flexible loop (residues 1313–1333) to form the pocket through water-mediated H-bonds with the peptide carbonyl groups of Q1314, K1327, S1328, and P1329 of the flexible loop. This loop-stabilizing role of R1225 observed in the PROTAC **2** and **3** complex structures is not seen in that of the PROTAC **1** ternary complex, where no bridging water molecules are observed in the gap between residue and loop (Fig. 5e). Other water-mediated H-bonds with the linker are formed by DCAF1 using the hydroxyl group of T1155 (blade 2, two rotamers modeled), and the peptide carbonyl groups of I1138 (blade 2) and T1139 (blade 2). No direct H-bonds occur between the PROTAC **3** linker and any WDR5 residues. However, as in the PROTAC **2** ternary complex, the side chains of K259 (blade 5–6 loop) and Y260 (blade 5–6 loop) of WDR5 interact with part of the linker through van der Waals and hydrophobic interactions.

The configuration of PROTAC **3** linker causes the blade 6 flexible loop (residues 1313–1333) of DCAF1 to move away in the crystal, as indicated by broken electron density for part of the loop (Fig. 5g). Residues 1317–1326 (DEDDLMEERM) of the loop were not modeled since their side chains could not be resolved, although electron density for backbone atoms for residues 1324–1326 (ERM) could be seen (Supplementary Fig. 9). This indicates that this loop remains part of the linker's binding surface while some of its constituting residues change side chain orientations, possibly using polar and/or negatively charged groups to interact with polar O atoms of the linker. A nearby flexible loop in blade 6 (residues 1372–1381) also forms part of the linker binding pocket, providing a van der Waals interactions surface. Several other residues of DCAF1 participate in van der Waals interactions with the PROTAC **3** linker, while fewer are made by those of WDR5. Due to the increased separation between DCAF1 and WDR5 in the complex, the binding interface is more porous, leaving the linker more deprotected from solvent than those of PROTAC **1** and **2** (Fig. 5a, g).

PROTAC 4 with a longer linker exhibits higher WDR5 degradation than PROTAC 1-3

The apparent unoccupied volume in PROTAC binding sites led us to hypothesize that a longer linker might occupy a larger space and render a more potent PROTAC. We therefore synthesized PROTAC **4**, containing a linker with nine PEG units (Fig. 6a). DSF (Supplementary Fig. 2) and SPR (Fig. 6b) also confirmed DCAF1·PROTAC4·WDR5 ternary complex formation. The observed binding cooperativity for PROTAC **1-3** was maximized for PROTAC **4** with a much larger decrease in SPR K_D value for PROTAC **4** binding to DCAF1 in the presence of WDR5 (5 ± 0.4 nM) in comparison with PROTAC **4** alone (59 ± 0.9 nM) (Table 1). Similarly, an increase of 14x in residence time for PROTAC **4** in the presence of WDR5 (k_{off} of 0.014 versus 0.001 1/s) indicated that PROTAC **4** also has the longest residence time among PROTAC **1-4** (Table 1). These improvements resulted in PROTAC **4** performing much better than PROTAC **1-3** in degrading the exogenous HiBiT-WDR5 with an EC_{50} of 40.2 ± 12.1 nM and a D_{max} of $73.8 \pm 2.9\%$ (Fig. 6c), almost reaching the D_{max} value ($78.7\% \pm 1.8\%$) of VHL-WDR5 PROTAC (MS67). However, EC_{50} for PROTAC **4** was higher than that for MS67 (3.8 ± 1.0 nM; Fig. 6d).

PROTAC **4** is our most effective WDR5 degrader in terms of D_{max}, achieving significant degradation. However, the endogenous D_{max} (49.1%) (Fig. 7a, b) was lower than the HiBiT exogenous D_{max} (73.8%). This pattern was consistent across all PROTACs tested (Fig. 3g–i). A possible explanation is that a fraction of the endogenous WDR5 might be inaccessible to the PROTAC, while being in complexes with other interacting proteins. In contrast, exogenous WDR5 being overexpressed, and not being part of such complexes, is more accessible, leading to more efficient degradation. To determine if the degradation of WDR5 by these PROTACs is proteasome-dependent, MV4-11 cells expressing HiBiT-tagged WDR5 were treated with PROTAC **4** at 1.5 μM (the concentration at which D_{max} was observed) (Fig. 7c). MG132, a proteasome inhibitor, was titrated and the amount of exogenous WDR5 was measured after 5 h. MG132 fully rescued the degraded HiBiT-WDR5 in a dose-dependent manner, reaching approximately 100%, confirming that PROTAC **4** induces proteasomal degradation (Fig. 7c). We also assessed the viability of MV4-11 cells after 5 days of treatment with PROTACs (Fig. 7d). We observed a dose-dependent decrease in cell viability in MV4-11 cells, as determined by the ATPlite assay. We used MS67 as a control, which exhibited the highest potency with an EC_{50} of 8.9 ± 2.6 nM, followed by PROTAC **4** with an EC_{50} of 158 ± 59 nM. PROTAC **3**, PROTAC **2**, and PROTAC **1** showed lower potencies, with EC_{50} values of 1455 ± 691 nM, 2487 ± 951 nM, and 3288 ± 646 nM, respectively. These results indicate that PROTAC MS67 and PROTAC 4 are more effective in reducing cell viability, potentially due to their higher WDR5 degradation compared to the other PROTACs. PROTAC **4** did not show a significant toxicity in MV4-11 cells expressing HiBiT WDR5 after 24 h (Supplementary Fig. 10a). MS67, however, displayed some toxicity after 24 h of treatment under the same conditions (Supplementary Fig. 10b).

We also orthogonally verified and confirmed the WDR5 endogenous degradation via Western blot analysis at PROTAC concentration with the maximum degradation (D_{max}) of the WDR5 (Fig. 7e). After 24 h treatment, MS67 and PROTAC **4** demonstrated comparable levels of WDR5 degradation, while PROTAC **1, 2**, and **3** showed moderate WDR5 degradation.

Structural basis for PROTAC 4 potency

We solved the crystal structure of PROTAC **4** ternary complex with DCAF1 and WDR5 to 2.07 Å and observed a similar orientation of WDR5 with respect to DCAF1 found in the PROTAC **2** and PROTAC **3** ternary complexes (r.m.s.d. of 0.2 Å) (Fig. 8a). Clear difference electron density indicated the presence of bound PROTAC **4** (Supplementary Fig. 11a), and high-resolution maps allowed precise mapping of its atoms except where electron density is weak, particularly at the second O atom of the
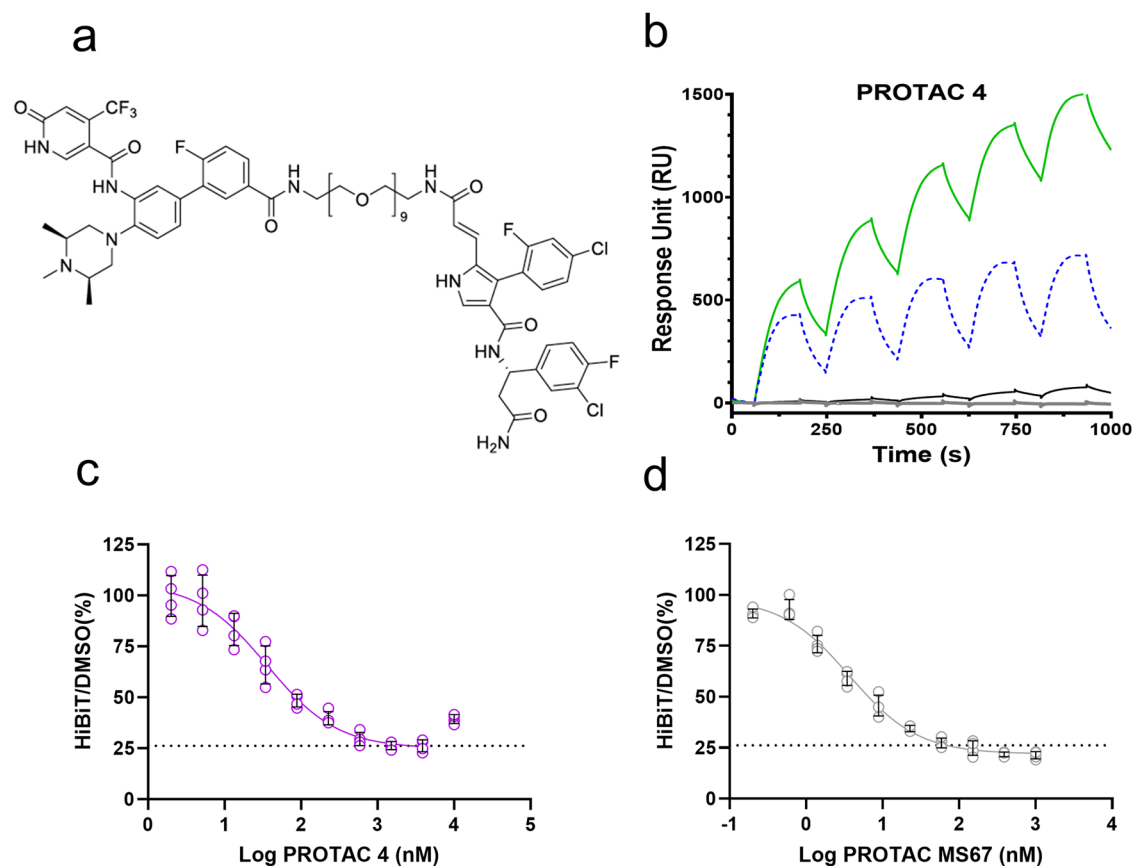
Fig. 6 | PROTAC 4 (OICR41114) degrades WDR5 better than PROTAC 1-3.
a PROTAC **4** chemical structure. **b** Confirmation of DCAF1-PROTAC **4**-WDR5 ternary complex formation by SPR. Experiments were performed the same as for PROTAC 1-3 in Fig. 3. Biotinylated DCAF1 was immobilized onto a sensor SA chip. A blank injection was used as a baseline (gray line). PROTAC **4** (black line) and WDR5 (dashed blue line) were injected independently before combining both in a 1:10 ratio of PROTAC with 0.25 μM WDR5 (green line) for ternary complex formation. In the presence of both WDR5 and PROTAC **4**, the binding response significantly increased. **c** PROTAC **4** degraded exogenous WDR5 in cells. The amount of WDR5 was quantified using the exogenous (HiBiT) WDR5 degradation assay as described in Methods. **d** PROTAC MS67 was used as a control and degraded HiBiT-WDR5 with an EC_{50} and D_{max} values of 3.8 ± 1.0 nM and $78.7 \pm 1.8\%$, respectively. Values are included as average $\pm$ SD of biological replicates ($n = 4$). Source data are provided as a Source Data file.

linker. Nevertheless, iterative refinement resulted in improved electron density maps and allowed the placement of all PROTAC **4** atoms by tracing the path of electron density with the lowest energy configuration of the linker chain. PROTAC **4** holds the ternary complex together and is compressed to an effective length of 38.9 Å to establish the DCAF1-WDR5 interface (Fig. 8b). A few weak interactions support the DCAF1-WDR5 interface which covers a surface area of ~520 Å². These include hydrophobic/van der Waals interactions between Q1158 (DCAF1 blade 2) and E151 (WDR5 blade 4), W1156 (DCAF1 blade 2) and Y191(WDR5 blade 4), and L1378 (DCAF1 blade 7) and N323 (WDR5 blade 7). A lone electrostatic/hydrogen bond also occurs between E1323 (DCAF1 blade 6) and K46 (WDR5 blade 7-1 loop) (Fig. 8c).

Compression of PROTAC **4** in the ternary complex is achieved by linker curving and coiling supported by various interactions with DCAF1 and WDR5 residues (Fig. 8d, Supplementary Fig. 11b). The curved portion of the linker proceeds from the DCAF1 anchor up to the fourth PEG unit, with a slight twist occurring at the third PEG unit. The PROTAC **4** linker curves in the opposite direction to that of PROTAC **3**. The rest of the linker (PEG units 5-9) forms a coil stacked against the WDR5 anchor and fills a hole bordered by WDR5 residues D107, Y131, F149, Y191, and Y260. Stabilizing this coiled section are electrostatic/hydrogen bonding interactions with an ordered water molecule situated just below the center of the coil, and the R1325 residue of DCAF1. Importantly, DCAF1 residues 1313-1333 assume a loop-helix-loop structure not seen in previously reported DCAF1 structures and our PROTAC **1-3** ternary complexes. This secondary structure is stabilized by various hydrogen bonding interactions between internal residues and with those of the adjacent loop (residues 1372–1381) (Supplementary Fig. 12). The loop-helix-loop structure bolsters the ternary complex through electrostatic interactions and van der Waals shape complementarity with the PROTAC **4** linker, including the coiled section sandwiched in between it and WDR5 (Fig. 8d). The greater potency of PROTAC **4** compared with PROTACs **1-3** likely stems from the relative structural stability of this ternary complex due to the above interactions. Protein interactions with DCAF1 and WDR5 anchors of PROTAC **4** are essentially conserved with those of PROTAC **1-3** (Supplementary Fig. 13).

Discussion

WDR5 is a highly networked, conserved nuclear scaffolding protein involved in the epigenetic regulation of histone modification and gene transcription as part of the MLL1 complex. Overexpression of WDR5 has been reported in various cancers including leukemia, breast, lung, and bladder cancers[39]. The anticancer effect of various WDR5-targeting antagonists that disrupt its interaction within the MLL complex has been evaluated[27,29,30]. However, WDR5 overexpression also affects the formation of a significant number of complexes and the function of other interacting proteins beyond MLL complexes. Therefore, depleting or reducing WDR5 levels in the cell by PROTAC-mediated proteasomal degradation could be a superior, or at least a complementary option to, the inhibition of MLL1-WDR5 interaction[4].

Since the discovery of PROTACs[6], only a few of E3 ligase receptors such as CRBN and VHL have been used. Recently, a CRBN-based
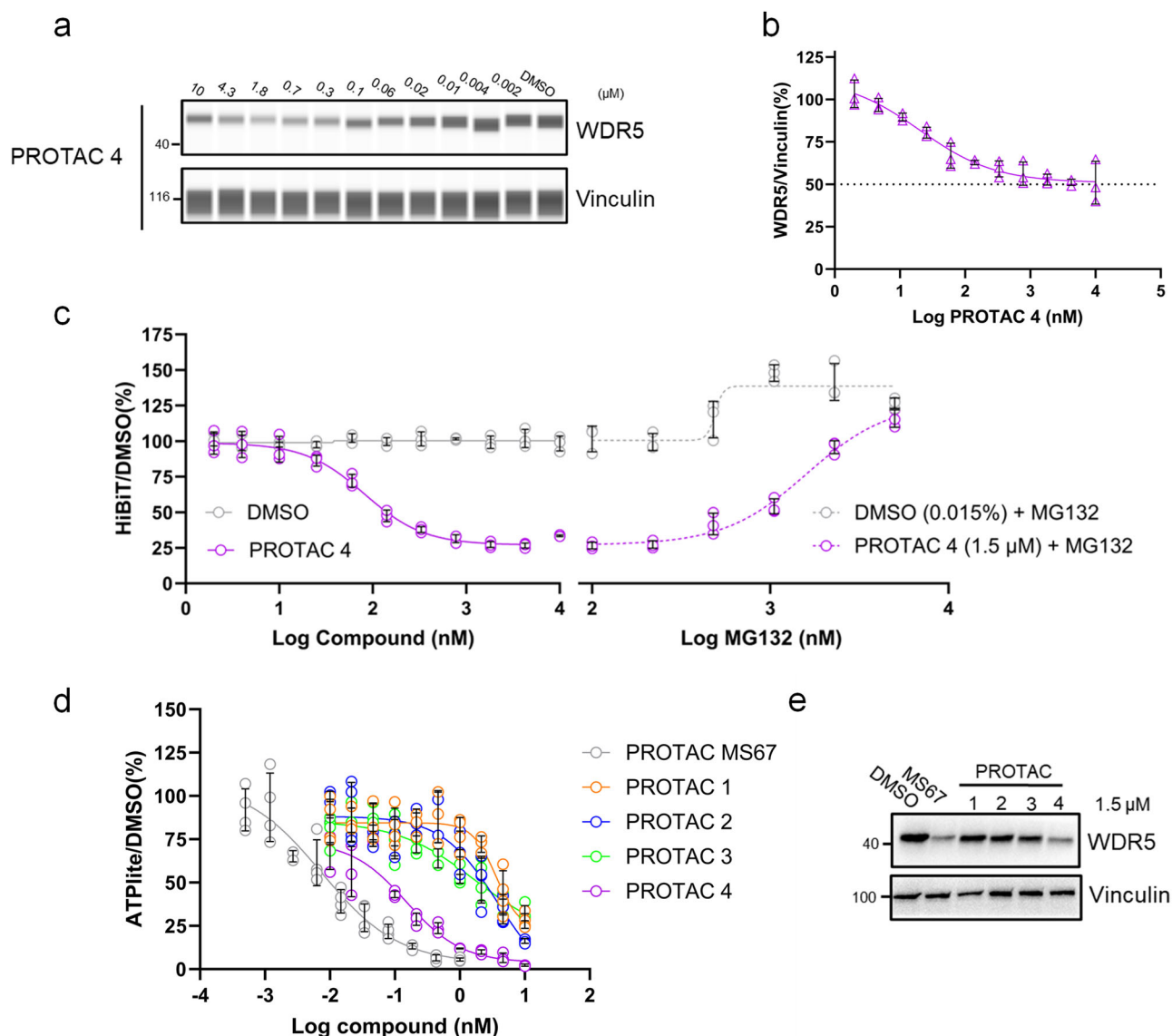
Fig. 7 | Degradation of the endogenous WDR5. The amount of WDR5 was quantified using the endogenous WDR5 degradation assays (ProteinSimple's Jess) as described in Methods. **a** A representative lane view image generated by Compass software, which is used to analyze simple western results. In MV4-11, PROTAC **4** degraded endogenous WDR5 in a dose-dependent manner after 24 h of treatment. Vinculin was used as a loading control. The concentration of PROTAC **4** is indicated above each lane. **b** PROTAC **4** degraded endogenous WDR5 with an EC_{50} and D_{max} values of 40 ± 24 nM and $49 \pm 1.9\%$, respectively. Values are included as average $\pm$ SD of biological replicates ($n = 3$). **c** PROTAC **4** degraded HiBiT-tagged WDR5 in a proteasome-dependent manner. MV4-11 cells expressing HiBiT tagged WDR5 were treated with PROTAC **4** for 5 h. PROTAC **4** decreased exogenous WDR5 in a dose dependent manner (purple circles). In the same plate but different wells, cells were co-treated with a fixed concentration of PROTAC **4** (1.5 μM) and increasing

concentrations of MG132 (purple dashed line) or with DMSO and MG132 (gray dashed line). MG132 fully rescued the levels of degraded HiBiT WDR5 after 5 h of PROTAC **4** and MG132 treatment. Values are included as average $\pm$ SD of biological replicates ($n = 3$). **d** ATPlite assay results showing the cytotoxic effects of DCAF1-WDR5 PROTACs on MV4-11 cells after 5 days of treatment. Cells were treated with varying concentrations of MS67 (control), PROTAC **1**, PROTAC **2**, PROTAC **3**, and PROTAC **4**. Cell viability was assessed using the ATPlite assay, and results were normalized to DMSO-treated controls. Values are included as average $\pm$ SD of biological replicates ($n \geq 4$). **e** Representative western blot image of 3 biological replicates. Western blot analysis was performed to assess the protein levels of WDR5 after 24 h of treatment of MV4-11 cells with 1.5 μM of PROTACs. MS67 and PROTAC **4** significantly decreased the levels of WDR5. Source data are provided as a Source Data file.

PROTAC targeting WDR5 (MS40), a dual WDR5 and Ikaros zinc finger (IKZF1 and IKZF3) transcription factor degrader, and a VHL-based WDR5 PROTAC (MS169) were reported[40]. The crystal structure of a quaternary complex of human WDR5 and pVHL:ElonginC:ElonginB bound to the PROTAC Homer (7Q2J) was also solved and characterized[41]. Despite these advancements, reports of CRBN down-regulation and mutation that cause resistance to immunomodulatory inhibitory drugs (IMiDs)[10,11] have increased the need for alternative essential E3 ligase receptors for PROTACs. DCAF1 is an essential protein and therefore could be a better alternative to the currently used E3 ligase substrate receptors such as CRBN for degradation of drug

targets[10]. In addition, the recently reported nanomolar ligands for DCAF1 further increase the suitability of this substrate receptor as an excellent candidate for PROTAC development[17,19].

In this work, we have developed DCAF1-based PROTACs that target WDR5 using ligands of the two proteins as anchors. Using PROTAC **1**, **2**, **3**, and **4**, the exogenous WDR5 was degraded with D_{max} of 32%, 41%, and 42%, 74%, respectively. These values were lower for endogenous WDR5 degradation (23–49%). Similar incomplete degradation levels of endogenous WDR5 have been previously reported[32,41]. For example, Schwalm and colleagues observed D_{max} of ~70% at the highest concentration of 7.5 μM for MS67 with no hook effect. They
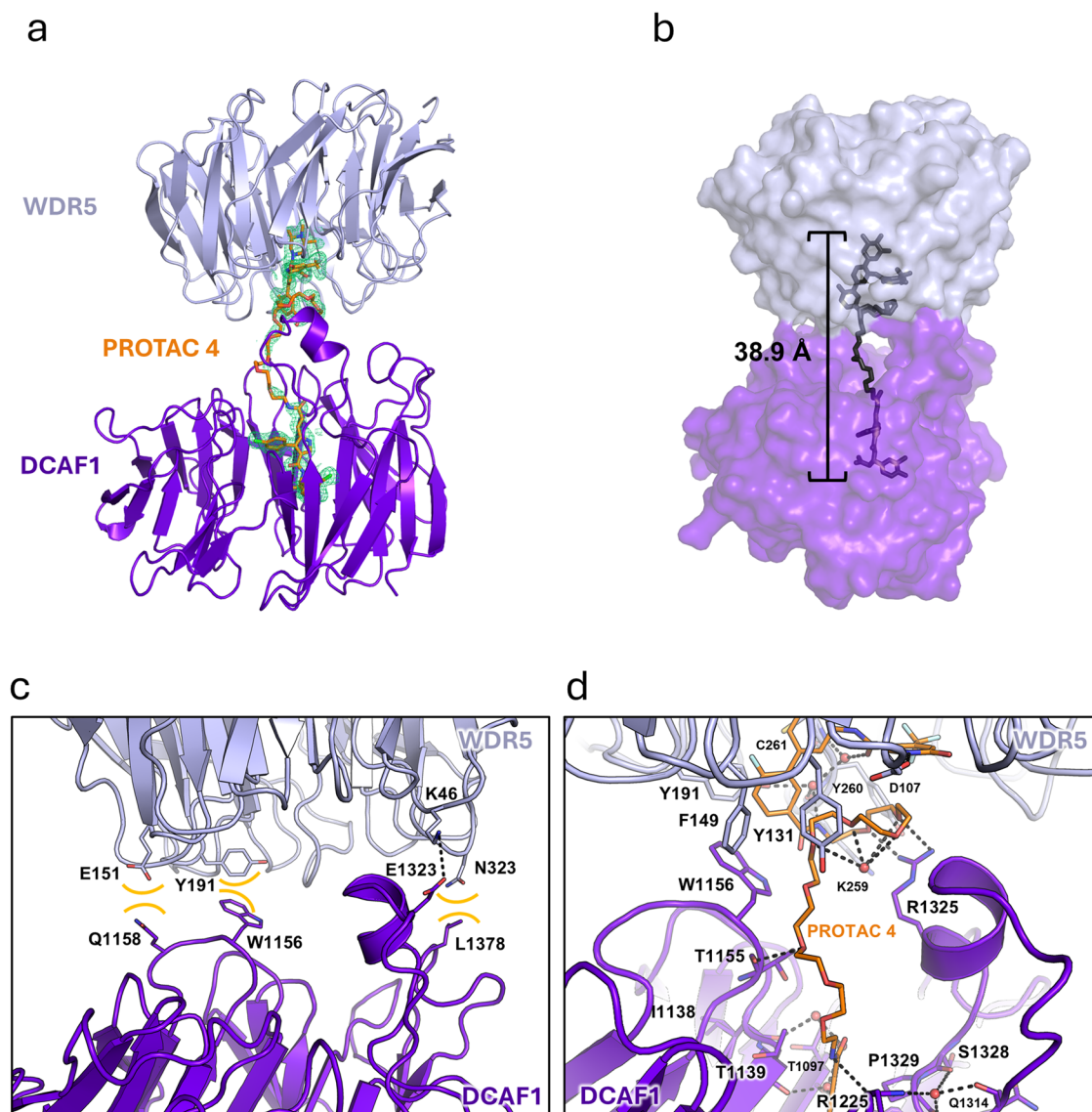
Fig. 8 | Crystal structure of the PROTAC 4 ternary complex with DCAF1 and WDR5. a Cartoon representation of the crystal structure showing PROTAC **4** (orange sticks), DCAF1 (purple) and WDR5 (blue). A $2F_o$-F_c electron density map contoured at 1.0σ surrounds PROTAC **4**. Unlike PROTAC **1-3**, PROTAC **4** forms a ternary complex with WDR5 and DCAF1 in which the latter's long loop (residues 1313–1333) forms a loop-helix-loop structure. **b** PROTAC **4** (black sticks) is compressed to an effective length of 38.9 Å, similar with those observed for PROTAC **1-3** in their ternary complexes. Surface representation indicates contacts between protein components enabled by PROTAC **4**. **c** Electrostatic/hydrogen bonding (broken black line) and hydrophobic/van der Waals interactions (brown concave lines) occur between the top side of the WDR domains of DCAF1 and WDR5 in the presence of PROTAC **4**. **d** The PROTAC **4** linker is accommodated inside the space formed by DCAF1 and WDR5 by coiling and compacting. A portion of the PROTAC **4**

linker close to the WDR5 anchor forms a coiled structure stabilized by an ordered water molecule (red sphere) located below the center of the coil, and interaction with the loop-helix-loop structure formed by residues 1313–1333. Specifically, R1325 of the loop-helix-loop structure of DCAF1 interacts with the coiled structure using hydrogen bonds. The coiled structure fills the space bordered by WDR5 residues D107, Y131, F149, Y191, and Y260. The coiled structure is further stabilized by water-mediated interactions with WDR5 residues and the WDR5 anchor of PROTAC **4** itself. The rest of the PROTAC **4** linker is curved and is also supported by the helix-loop-helix structure of DCAF1. Near the DCAF1 anchor, several water-mediated interactions with DCAF1 residues stabilize the linker conformation. As is also seen in the PROTAC **2** and PROTAC **3** ternary complexes, residue R1225 helps stabilize the linker and the base of the loop-helix-loop structure through direct and water-mediated hydrogen bonding interactions.

also noted that none of the other WDR5 degraders that they tested were able to completely eliminate WDR5[41]. It was further suggested that the level of degradation may be cell-line dependent[41]. For PROTAC **1-4** we observed the hook effect starting at 10 μM. These observations could be the result of outcompeting ternary complex formation by binary complexes with PROTACs, and/or lower concentrations of endogenous DCAF1 than WDR5. Other reasons include the possibility that a significant number of WDR5 molecules are in protein complexes protected by chromatin[42], or that WDR5 is replenished quickly as degradation reached equilibrium[41], or that the PROTACs did not efficiently penetrate the nucleus.

We also presented the crystallographic ternary structures of DCAF1-based PROTACs with WDR5. While the protein anchors bind DCAF1 and WDR5 in a conserved manner, the linkers exhibited different length-dependent conformations inside the DCAF1-WDR5 interface although with similar effective lengths of about 39 Å. It appears that the effective PROTAC length is determined by the available binding space between DCAF1 and WDR5 in the most stable configuration(s) of the ternary complex. As a corollary to this, a linker length limit exists at which the PROTAC can no longer fit inside the binding space and DCAF1 and WDR5 can no longer form stable ternary complexes, leading to less WDR5 degradation in the cell. Conversely, PROTACs with shorter linkers
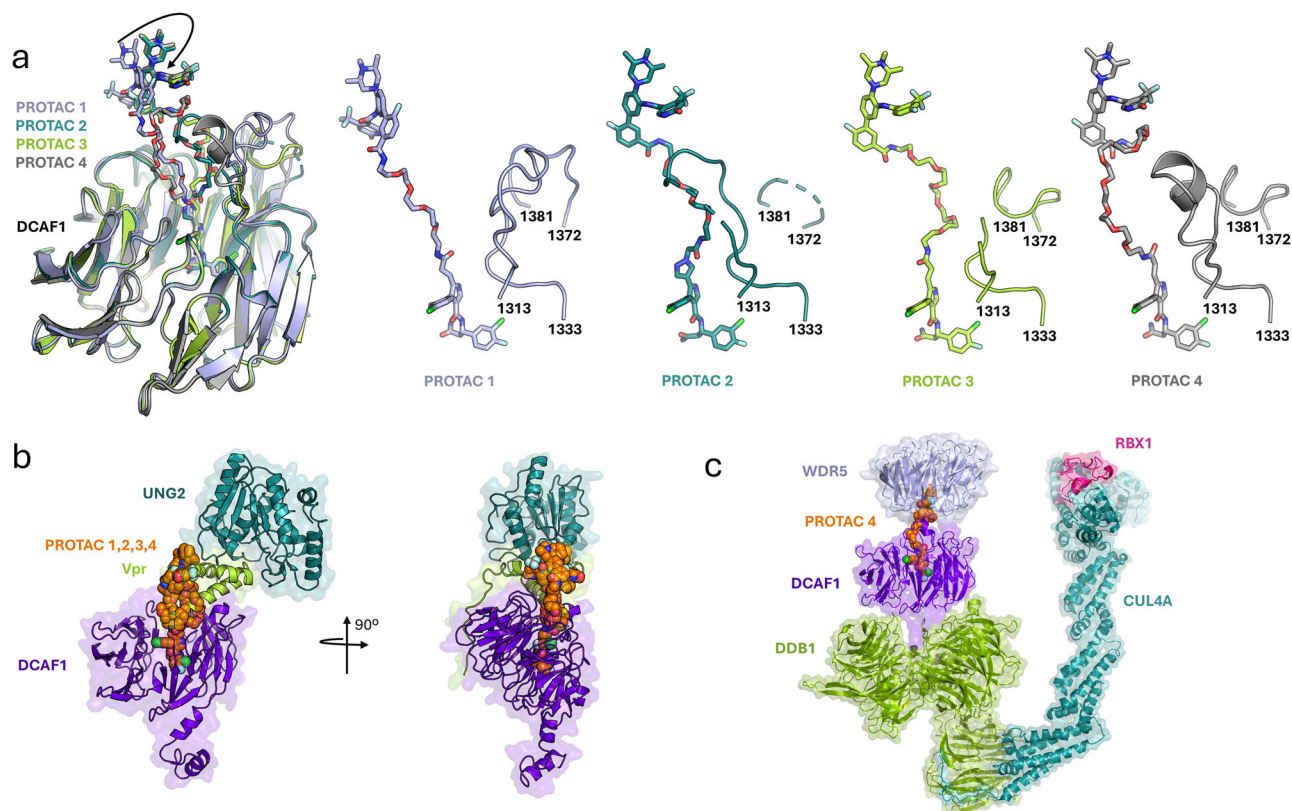
Fig. 9 | DCAF1 uses flexible loops for substrate recognition. a Superposition of DCAF1 component of ternary complexes shows rotation of the WDR anchor in the PROTAC **2**, **3**, and **4** complexes relative to that of PROTAC **1**. In response to PROTAC linker length and curvature, DCAF1's specificity loop (residues 1313-1333) rearranges to accommodate it, as shown in the series of structures on the right. A nearby loop (residues 1372-1381) in blade 7 also changes conformations. Here, each PROTAC-DCAF1 pair is colored the same: PROTAC **1**-DCAF1 is light blue, PROTAC **2**-DCAF1 is teal, PROTAC **3**-DCAF1 is yellow green, PROTAC **4**-DCAF1 is gray. **b** Superposition of PROTAC ternary complex structures with that of DCAF1-Vpr-UNG2 complex (PDB id 5JK7, DDB1 is not shown for clarity) shows that PROTAC **1**, **2**,

3, and **4** (spheres) together partially occupy the Vpr (yellow green cartoon) volume between DCAF1 (purple) and UNG2 (teal). PROTACs with longer linkers may fill the extra volume and lead to more stable ternary complexes and exhibit greater efficiency. **c** Superposition of the PROTAC **4** ternary complex structure with that of DDB1-DCAF1-CUL4A-RBX1 complex orientates WDR5 for ubiquitination by the E3 ligase. DCAF1 and WDR5 are colored as in Fig. 8a, DDB1 is moss green, CUL4A is teal, RBX1 is magenta. PROTAC **4** is shown as spheres. The extra surface for DCAF1 (purple) inserted into the DDB1 adaptor corresponds to the N-terminus that is removed from the crystallized sequence of DCAF1.

than PROTAC **1** may also be unable to form stable ternary complexes due to insufficient separation between DCAF1 and WDR5, forcing an energetically unfavorable collision between them. Indeed, our collective data on PROTAC **5** with a linker shorter than that of PROTAC **1**, support this hypothesis (Supplementary Fig. 14–18). Similar to PROTAC **1-4**, PROTAC **5** also binds to DCAF1 (SPR K_D of 15.2 ± 2 nM) and WDR5 (SPR K_D of 26.4 ± 4 nM), which were orthogonally confirmed by DSF (Supplementary Fig. 15–16). PROTAC **5** even stabilized both DCAF1 and WDR5 in a mixture when tested at equimolar concentration, indicating the ability to bind to both proteins at the same time. SPR supported the formation of a ternary complex by PROTAC **5** although less efficiently than PROTAC **2**, **3** and **4** (Table 1, Fig. 3a–c, Fig. 6b, Supplementary Fig. 16). However, PROTAC **5** did not degrade exogenous or endogenous WDR5 in cells (Supplementary Fig. 17). We did solve the crystal structure of a DCAF1-WDR5 binary complex from a crystal grown in the presence of PROTAC **5** (Supplementary Fig. 18, Supplementary Table 1). However, the crystal structure was devoid of bound PROTAC **5**, indicating the ternary complex probably was not stable enough (Supplementary Fig. 18a). Few non-covalent interactions, one of which involves the E1324 residue in the DCAF1's long loop, stabilize the observed (DCAF1) top-to-(WDR5) bottom configuration that is unlike the top-to-top configuration expected of an active PROTAC (Supplementary Fig. 18b, c). Although no electron density was observed for PROTAC **5** in this structure, it appears to have brought DCAF1 and WDR5 together stably enough to co-crystallize. DCAF1 and WDR5 did not co-crystallize in the absence of

PROTAC **5** (control experiment), further supporting a role for PROTAC **5** in the binary complex formation in the crystal. Lack of complex stability is likely a major factor in this case. Indeed, protein B-factors of the binary complex suggest greater positional disorder for WDR5 indicating its greater mobility than DCAF1 in the complex (Supplementary Fig. 18d).

Interestingly, the crystal structures also revealed a DCAF1 specificity loop, which organizes into a loop-helix-loop structure in the presence of PROTAC **4** but assumes other configurations with weaker PROTAC **1-3**. The specificity loop, in tandem with a shorter adjacent loop, adjusts to the different shapes of PROTAC-WDR5 pairs by rearranging to remodel its binding surfaces (Fig. 9a). In contrast, other parts of DCAF1, including other loops on its substrate-receiving face, maintain a fairly conserved architecture across the ternary complexes. Indeed, examination of residue B-factors in the PROTAC **1** ternary complex where all cloned internal residues are present in the model shows that the above loops have significantly higher B-factors than the rest of the protein (Supplementary Fig. 19). In the same complex, the secondary structures of WDR5 that bind directly to DCAF1 remain quite rigid, indicating that it is the binding face of DCAF1 that adapts to the PROTAC-WDR5 substrate using the specificity loop. Furthermore, in the DCAF1-WDR5 binary complex, the same flexible loops readjust to recognize a different face of WDR5 (Supplementary Fig. 18a–d). Thus, the five crystal structures herein provide structural evidence for the role of flexible loops in PROTAC-WDR5 recognition, and possibly, in the recognition of endogenous substrates of E3 ligases that use DCAF1 as a receptor.

Comparison of the ternary structures with that of the DDB1-DCAF1-Vpr-UNG2 complex presents future opportunities for PROTAC design. Superposition of the five complexes shows that PROTAC **1-4** collectively occupy approximately 50% of the volume occupied by the viral protein Vpr (-7500 Å^3 for residues 18-74[43]) in the latter's quaternary complex (Fig. 9b). Next generation PROTACs bearing longer, or bulkier enough linkers may be able to fill the remaining volume occupied by Vpr (Supplementary Fig. 20). Alternatively, greater ternary complex stability could be achieved with PROTAC moieties that better complement the shape of DCAF1's loop-helix-loop structure to bind WDR5 together.

Placement of the PROTAC ternary complexes within the structure of the DDB1-DCAF1-CUL4A-RBX1 complex poises WDR5 for ubiquitination by the E3 ligase (Fig. 9c, Supplementary Fig. 21a–c). The greater tilt of WDR5 in the PROTAC **1** ternary complex compared to those in the PROTAC **2-4** ternary complexes appear to bring it closer to the putative position of E2. However, this WDR5 orientation does not translate to greater PROTAC cellular activity, since PROTAC **4** results in more pronounced degradation of both exogenous and endogenous WDR5 in cells. Either observed WDR5 orientation can present surface lysine residues for ubiquitination (Supplementary Fig. 22). The difference in degradation efficiency between PROTAC **1** and PROTAC **4** therefore likely arises from the relative stability of their ternary complexes.

In conclusion, we discovered four DCAF1-WDR5 PROTACs that targeted WDR5 for degradation in the cell. We also solved crystal structures of their ternary complexes that provided valuable insights into the interaction of WDR5 and DCAF1 and elucidated the dynamic role of DCAF1 loops in recognizing and interacting with WDR5-PROTACs and possibly, endogenous DCAF1 substrates. The ternary structures bearing PROTACs of different lengths can be used as a guide to design more active PROTACs that lead to stable complexes with optimal geometry within the E3 ligase. Overall, our results also further validate DCAF1 as a versatile E3 ligase receptor in the development of novel PROTACs[10].

Methods
Protein expression in *Sf9* cells (baculovirus expression system)
A pFastBacDual vector containing the coding sequence for N-terminal His-tagged DCAF1(1077-1390) was designed in house under polyhedrin promoter control, then purchased from ThermoFisher Scientific. The vector was transformed into DH10Bac *Escherichia coli* (*E. coli*; ThermoFisher; Cat. #10361012) to create, amplify, and isolate the bacmid DNA of interest, according to a protocol by Hutchinson & Seitova (2021)[44]. Using the same protocol, recombinant baculovirus carrying the code for the proteins-of-interest were produced to infect large-scale suspension cultures. In short, Spodoptera frugiperda 9 (*Sf9*) cells (ThermoFisher; Cat. #11496015) maintained in a 6-well plate format (ThermoFisher; Cat. #140685) were transfected (VWR; Cat. #CA89129-920; according to manufacturer's instructions) with the harvested bacmid DNA, generating recombinant baculovirus. This virus was collected and subsequently utilized to infect larger quantities (>2 L) of *Sf9* suspension culture. After approximately 48–72 h of incubation, a culture pellet was collected via centrifugation and stored at −80 °C until required for protein purification.

Protein expression in *E. coli* cells
N-His-tagged WDR5 (24-334) cloned in pET28-MHL vector was provided by Structural Genomics Consortium[45], Toronto, Canada. The construct was transformed into *E. coli* BL21-Codonplus (DE3)-RIL competent cells (VWR; Cat. #230245). An overnight starter culture was grown in LB (Sigma; Cat. #L3022-1KG) supplemented with kanamycin (VWR; Cat. # CA45000-640) and chloramphenicol (+KC; Sigma-Aldrich; Cat. # C0378), then used to inoculate TB media (Sigma; Cat. #T9179) + KC. Cultures were grown at 37 °C until an OD$_{600}$ reading of 0.8 was reached, at which point the temperature was lowered to 18 °C.

At this point, 0.5 mM IPTG (Bioshop; Cat. #IPT002.50) was added to induce protein expression using a LEX bioreactor system (Epiphyte3; Model #Lex-24). Cultures were allowed to grow overnight, and the cells were then harvested by centrifugation. The resultant cell pellets were stored at −80 °C until required for protein purification.

Protein purification
Sf9 cell pellets were resuspended in binding buffer: a pH 7.5, 50 mM Tris-HCl buffer, containing 500 mM NaCl, 5 mM imidazole, and 5% glycerol (Bioshop; Cat. #s TRS002.5, SOD001.5, IMD508.1, and GLY004.4, respectively). The cell suspension was supplemented with 100 mM benzamidine (Bioshop; Cat. # BEN601.100), 100 mM PMSF (Bioshop; Cat.# PMS123.100), 10 mM MgCl$_2$, 1 mM Tris(2-carboxyethyl) phosphine hydrochloride (TCEP), 1X protease inhibitor cocktail (0.25 mg/ml aprotinin, 0.25 mg/ml leupeptin, 0.25 mg/ml pepstatin A and 0.25 mg/ml E-64; Sigma; Cat. #s 208337-1KG, C4706-50G, 11583794001, 11529048001, 11524488001, and 11585681001, correspondingly) and 1X Roche complete EDTA-free protease inhibitor cocktail tablet (ThermoFisher; Cat. #PIA32955). The cells were lysed chemically with NP40 at a final concentration of 0.5 % (ThermoFisher; Cat. #PI85124) and 120 unit/L benzonase nuclease (Sigma; Cat. #E1014-25KU), followed by sonication via a Qsonica 700 (ThermoFisher; Cat. #15338281) set to 70% amplitude (10 s on; 7 s off). The crude extract was clarified by high-speed centrifugation (20 min at 16,000 rpm, 4 °C), at which point the clarified lysate was then passed through a Hispur™ Ni-NTA resin (ThermoFisher; Cat. #88223) column pre-equilibrated with binding buffer. The column was then washed and eluted with wash and elution buffers (same as binding buffer but containing additional imidazole at final concentrations of 30 mM and 250 mM, respectively). The protein was further purified by gel filtration on a Superdex 200 26/60 (Cytiva; Cat. #28989336) using a BioRad system (BioRad; Cat. #7880009) pre-equilibrated with 50 mM Tris 7.5, 150 mM NaCl, 5% glycerol, and 1 mM TCEP. The purity of the fractions was confirmed via SDS-PAGE, whereafter pure fractions were pooled, concentrated, and flash frozen.

Collected *E. coli* pellets were resuspended in binding buffer (50 mM Tris-HCl, 500 mM NaCl, 5 mM imidazole, 1 mM MgCl$_2$, and 1 mM TCEP, supplemented with 100 mM benzamidine, 100 mM PMSF, 1X protease-inhibitor cocktail, and 1X Roche complete EDTA-free protease-inhibitor cocktail tablet). The cells were lysed chemically with 0.5% CHAPS (Sigma; Cat. #C3023-100G) and 5 µl/L benzonase nuclease, followed by sonication with a Qsonica 700 at an amplitude of 80% (10 s on; 7 s off). The crude extract was subsequently clarified by high-speed centrifugation (20 min at 16,000 rpm, 4 °C), and the resultant supernatant was passed through a pre-equilibrated Hispur™ Ni-NTA resin column pre-equilibrated with binding buffer. To collect the protein, the column was first washed with binding buffer containing 30 mM imidazole, followed by elution containing 300 mM imidazole. The eluent was dialyzed overnight in 50 mM Tris-HCl, 150 mM NaCl, 5% glycerol, and 1 mM TCEP at a final pH of 7.5. Dialyzed fractions were pooled, concentrated and flash frozen.

Surface plasmon resonance to measure PROTAC binding to DCAF1 or WDR5
All SPR experiments were performed using a Biacore T200 instrument and an S-series Streptavidin (SA) sensor chip (Cytiva; Cat. #29104992). A single chip was used to immobilize biotinylated DCAF1 and WDR5 in the following buffer: 0.01 M HEPES (ThermoFisher; Cat. #A14777.30) pH 7.4, 0.15 M NaCl, 0.005% v/v Surfactant P20. The two proteins were immobilized in different channels to a signal ranging between 7000–9000 RU. All binding experiments were performed in HBS-P buffer: 0.01 M HEPES pH 7.4, 0.15 M NaCl, 0.005% v/v Surfactant P20 with 5% DMSO. Compounds were injected for 60 s followed by buffer for 600 s at a flow rate of 40 µl/min. Compounds were injected in a concentration titration series of 0.192, 0.096, 0.048, 0.024, and

0.012 μM for 60 s at a flow rate of 40 μl/min followed by a dissociation time of 600 s. All experiments were performed in triplicate. Blank-subtracted sensorgrams were used to extract the maximum response and compound K_D, on-rate (k_{on}), off-rate (k_{off}) and R_{max} were measured using kinetic curve fitting.

Surface plasmon resonance to assess ternary complex formation

All SPR experiments were performed using a Biacore T200 instrument and a S-series SA (Streptavidin) sensor chip. A single chip was used to immobilize biotinylated DCAF1 in the buffer: 0.01 M HEPES pH 7.4, 0.15 M NaCl, 0.005% v/v Surfactant P20. The protein was immobilized in three channels to a signal ranging between 5000–5500 RU. All binding experiments were performed in HBS-P buffer: 0.01 M HEPES pH 7.4, 0.15 M NaCl, and 0.005% v/v Surfactant P20 with 5% DMSO. Compounds were injected alone or in the presence of 0.25 μM of unbiotinylated WDR5 protein. Compounds were injected in a concentration titration series with a top concentration of 0.192 μM and titrated 2-fold down to yield a total of 5 concentrations. Single cycle kinetics was used with an association time of 120 s with a flow rate of 20 μl/min followed by a dissociation time of 600 s. All experiments were performed in triplicate. Blank-subtracted sensorgrams were used to extract the maximum response and compounds' K_D, on-rate (k_{on}), off-rate (k_{off}) and R_{max} values were calculated using kinetic curve fitting with a 1:1 binding model in Biacore T200 Evaluation software.

Differential scanning fluorimetry assay to detect PROTAC binding

DSF experiments were performed using an Applied Biosystems™ QuantStudio™ 5 Real-Time PCR System. Reactions (200 μL) contained 0.2 mg/mL DCAF1 or WDR5 alone with either 0.5% DMSO or 5.5 μM PROTAC in DSF buffer (100 mM HEPES pH 7.5 and 150 mM NaCl) and 5X SYPRO Orange (Invitrogen, Cat# S6650). Reactions (200 μL) which contained both DCAF1 and WDR5 with PROTAC were first incubated at a 1:1:1 ratio of 5.5 μM for 20 min at room temperature in DSF buffer before the addition of 5X SYPRO Orange. Reactions were aliquoted into 20 μL per well in a MicroAmp™ EnduraPlate™ Optical 384-well plate (Applied Biosystems, Cat# A36931) and sealed with MicroAmp™ Optical Adhesive Film (Applied Biosystems, Cat# 4311971). Each reaction had 8 replicates with final concentration of 0.5% DMSO. Thermal denaturation was monitored from 25 °C to 95 °C at a rate of 0.066 °C increase per second and data points were collected every second. Collected data was analyzed using Protein Thermal Shift™ Software v1.4 and was replotted for presentation using GraphPad Prism 10.2.

Exogenous HiBiT WDR5 degradation assay

MV4-11 cells engineered to express HiBiT-tagged WDR5 (Hb-WDR5) were plated across a 96-well plate at a density of 20,000 cells per 100 μL in RPMI medium (ThermoFisher; Cat. #11875093) supplemented with 10% FBS (ThermoFisher; Cat. #12483020). A range of 12 different concentrations of compounds (10 μM to 0.002 μM) were added using an HP D300e Digital Dispenser (Tecan; Model # 30100152). The cells were incubated at 37 °C in a 5% CO₂ for 24 h. Subsequently, Nano-Glo HiBiT Lytic Reagent (Promega, Cat. #N3030) containing both LgBiT protein and the furimazine substrate was added to the wells. The HiBiT and LgBiT proteins interact to form a luminescent NanoLuc luciferase enzyme, which emits light in the presence of the furimazine substrate. The intensity of luminescence emitted is directly proportional to the amount of HiBiT-tagged WDR5 present. Plates were shaken on an orbital shaker at 500 rpm for 10 min, followed by luminescence measurement using a Cytation 3 plate reader (BioTek, Model #CYTV3). The ATPlite 1step Luminescence Assay System (PerkinElmer, cat# 6016739) was used to measure ATP levels, which served as an indirect measure of cell viability. To measure ATP levels, 100 μL of reconstituted ATPlite reagent (containing luciferase and D-luciferin) was added to cells in a 96-well plate corresponding to the layout used for the HiBiT degradation assay. The plate was then shaken for 10 min to ensure thorough mixing. Luminescence signal was measured using the Cytation 3 plate reader (BioTek).

Cell culture

MV4-11 cells were purchased from the American Type Culture Collection (ATCC). Cells were cultured in RPMI (Life Tech, 11875-119) supplemented with 10% FBS (Corning, 35075CV) at 37 °C in a 5% CO₂ incubator. Cells provided by the ATCC were routinely authenticated using short tandem repeat.

Endogenous WDR5 degradation assay using ProteinSimple's Jess

Parental MV4-11 cells were seeded in a 12-well plate at a density of 0.5 million cells/mL in RPMI medium supplemented with 10% FBS. The HP D300e Digital Dispenser was used to deliver 11 different concentrations of the compounds (10 μM to 0.002 μM). Following a 24-h incubation period at 37 °C with 5% CO₂, cells were collected and centrifuged at $300 \times g$ for 10 min. The cell pellet was washed with cold PBS and subjected to a further centrifugation at $300 \times g$ for 10 min. Cell lysis was performed using a buffer containing 1% NP-40 in PBS supplemented with 1X Halt protease and phosphatase inhibitor cocktail (ThermoFisher; Cat. # 78444). The Jess System (ProteinSimple; JS4296), which automates the traditional western blot process, was employed to detect and quantify the levels of endogenous WDR5 (https://www.bio-techne.com/p/simple-western/jess-automated-western-blot-system_004-650).

Western blot

MV4-11 cells were trypsinized and pelleted by centrifugation at $500 \times g$ for 5 min. Cells were lysed using M-PER lysis buffer (ThermoFisher, cat# 78501), 1% SDS, and 1X Halt protease and phosphatase inhibitor cocktail (ThermoFisher, Cat# 78444). The lysate was sonicated, centrifuged for 10 min at $10,000 \times g$, and transferred to a new 1.5 mL Eppendorf tube. The Colorimetric DC Protein Assay (BioRad, 500-0207) was used to quantify the amount of protein in each lysate. Sodium dodecyl sulfate–polyacrylamide gel electrophoresis (SDS-PAGE) was used to run and separate the samples. The iBlot2 transfer system (Invitrogen, Model IB21001) was used to transfer the samples onto a polyvinylidene difluoride (PVDF) membrane (Invitrogen; Cat. #IB24001). Anti-WDR5 (1:1000; CST, Cat# 13105, lot#3), and anti-Vinculin (1:1000, CST, Cat#13901, lot:9) were used to detect the respective proteins and HRP-conjugated goat anti-rabbit secondary antibody (Bio-Rad, 1706515, 1:10,000) was used to detect the primary antibodies. After the addition of immobilon chemiluminescent HRP substrate (Thermo Scientific), ChemiDoc imager was used to visualize the different bands on the membrane.

Crystallization and structure determination of PROTAC ternary complexes

To assemble complexes, 200 μM of purified DCAF1 was incubated on ice with 200 μM of PROTAC 1, 2, 3, 4 or 5 for 1 h, followed by the addition of 200 μM purified WDR5. The ternary complex mixture of 1:1:1 DCAF1: PROTAC: WDR5 was incubated on ice for another hour, then concentrated by centrifugation to bring the protein concentrations back to 200 μM. Sitting drop crystallization trays were immediately prepared for the complexes using commercial screens (Hampton Research) on the Gryphon crystallization robot (Art Robbins Instruments). Trays were stored at 21 °C. Crystals of complexes were observed after three days and grew to maximum dimensions within a week. Large crystals of each complex were observed in various conditions. Crystals were frozen in liquid nitrogen using 30% glycerol as cryoprotectant, then sent to the Canadian Light Source for data collection at $\lambda = 1.18061$ Å (CMCF-BM line) (PROTAC 1–3 ternary complexes and DCAF1-WDR5 binary complex) or collected locally using the

Rigaku MicroMax-003 (λ = 1.54189 Å) with an Eiger R 1 M detector. The best diffraction data were collected from a single crystal grown in 5% w/v 1-ethyl-3-methylimidazolium ethyl sulfate, 15% w/v polyethylene glycol 20,000, pH 7.9 (PROTAC 1 ternary complex), 0.1 M sodium acetate trihydrate, pH 4.6, 2.0 M sodium formate (PROTAC 2 ternary complex), 35% v/v tacsimate, pH 7.0 (PROTAC 3 ternary complex), 1.8 M Sodium phosphate monobasic monohydrate, potassium phosphate dibasic/pH 6.9 (PROTAC 4 ternary complex), and 0.2 M imidazole, pH 7.4, 20% w/v polyethylene glycol 4000 (DCAF1-WDR5 binary complex). Diffraction data were indexed, integrated, and scaled using XDS or CrysAlis[Pro] (Rigaku, Agilent Technologies; https://rigaku.com) and Aimless (CCP4) (https://journals.iucr.org/d/issues/2023/06/00/ai5011/index.html)[46]. The structure of each complex was solved by molecular replacement in Phenix Phaser[47], using the apo structures of DCAF1 (PDB id 8F8E) and WDR5 (PDB id 2GNQ) as search models. Each structure was initially refined in PHENIX with simulated annealing and coordinate shaking to remove model bias. Subsequent model building and refinement were performed in COOT[48] and PHENIX using individual coordinate, occupancy, and B-factor optimization. Data collection and refinement statistics are summarized in Supplementary Table 1.

Reporting summary
Further information on research design is available in the Nature Portfolio Reporting Summary linked to this article.

Data availability
Source data are provided with this paper as a Source Data. The refined coordinates and data for the co-crystal structures were deposited and available in the PDB with the accession codes of 9B9H, 9B9T, 9B9W, 9DLW, and 9BA2. For Figs. 3a–i, 6b–d, 7a–e and Supplementary information Figs. 2a–d, 4a–c, 15a, b and 16, the Source Data are provided as a Source Data file. Any other data are available from the authors. Source data are provided with this paper.

References
1. Scheer, S. et al. A chemical biology toolbox to study protein methyltransferases and epigenetic signaling. *Nat. Commun.* **10**, 19 (2019).
2. Wu, Q. et al. A chemical toolbox for the study of bromodomains and epigenetic signaling. *Nat. Commun.* **10**, 1915 (2019).
3. Cui, Q., Huang, C., Liu, J. Y. & Zhang, J. T. Small molecule inhibitors targeting the "Undruggable" survivin: the past, present, and future from a medicinal chemist's perspective. *J. Med. Chem.* **66**, 16515–16545 (2023).
4. Poso, A. The future of medicinal chemistry, PROTAC, and undruggable drug targets. *J. Med. Chem.* **64**, 10680–10681 (2021).
5. Sakamoto, K. M. et al. Protacs: chimeric molecules that target proteins to the Skp1-Cullin-F box complex for ubiquitination and degradation. *Proc. Natl Acad. Sci. USA* **98**, 8554–8559 (2001).
6. Li, X. & Song, Y. Proteolysis-targeting chimera (PROTAC) for targeted protein degradation and cancer therapy. *J. Hematol. Oncol.* **13**, 50 (2020).
7. Zheng, N. & Shabek, N. Ubiquitin ligases: structure, function, and regulation. *Annu. Rev. Biochem.* **86**, 129–157 (2017).
8. Cieslak, M. & Slowianek, M. Cereblon-recruiting PROTACs: will new drugs have to face old challenges? *Pharmaceutics* **15**, 812 (2023).
9. Jiang, H., Xiong, H., Gu, S. X. & Wang, M. E3 ligase ligand optimization of Clinical PROTACs. *Front. Chem.* **11**, 1098331 (2023).
10. Schroder, M. et al. DCAF1-based PROTACs with activity against clinically validated targets overcoming intrinsic- and acquired-degrader resistance. *Nat. Commun.* **15**, 275 (2024).
11. Hanzl, A. et al. Functional E3 ligase hotspots and resistance mechanisms to small-molecule degraders. *Nat. Chem. Biol.* **19**, 323–333 (2023).
12. Lee, J. et al. Discovery of E3 ligase ligands for target protein degradation. *Molecules* **27**, 6515 (2022).
13. Zhang, S., Feng, Y., Narayan, O. & Zhao, L. J. Cytoplasmic retention of HIV-1 regulatory protein Vpr by protein-protein interaction with a novel human cytoplasmic protein VprBP. *Gene* **263**, 131–140 (2001).
14. Jung, H. Y., Wang, X., Jun, S. & Park, J. I. Dyrk2-associated EDD-DDB1-VprBP E3 ligase inhibits telomerase by TERT degradation. *J. Biol. Chem.* **288**, 7252–7262 (2013).
15. Hossain, D., Javadi Esfehani, Y., Das, A. & Tsang, W. Y. Cep78 controls centrosome homeostasis by inhibiting EDD-DYRK2-DDB1(Vpr)(BP). *EMBO Rep.* **18**, 632–644 (2017).
16. Schabla, N. M., Mondal, K. & Swanson, P. C. DCAF1 (VprBP): emerging physiological roles for a unique dual-service E3 ubiquitin ligase substrate receptor. *J. Mol. Cell Biol.* **11**, 725–735 (2019).
17. Li, A. S. M. et al. Discovery of nanomolar DCAF1 small molecule ligands. *J. Med. Chem.* **66**, 5041–5060 (2023).
18. Tao, Y. et al. Targeted protein degradation by electrophilic PROTACs that stereoselectively and site-specifically engage DCAF1. *J. Am. Chem. Soc.* **144**, 18688–18699 (2022).
19. Vulpetti, A. et al. Discovery of new binders for DCAF1, an emerging ligase target in the targeted protein degradation field. *ACS Med. Chem. Lett.* **14**, 949–954 (2023).
20. Guarnaccia, A. D. & Tansey, W. P. Moonlighting with WDR5: a cellular multitasker. *J. Clin. Med.* **7**, 21 (2018).
21. Vedadi, M. et al. Targeting human SET1/MLL family of proteins. *Protein Sci.* **26**, 662–676 (2017).
22. Grebien, F. et al. Pharmacological targeting of the Wdr5-MLL interaction in C/EBPalpha N-terminal leukemia. *Nat. Chem. Biol.* **11**, 571–578 (2015).
23. Senisterra, G. et al. Small-molecule inhibition of MLL activity by disruption of its interaction with WDR5. *Biochem. J.* **449**, 151–159 (2013).
24. Cao, F. et al. Targeting MLL1 H3K4 methyltransferase activity in mixed-lineage leukemia. *Mol. Cell* **53**, 247–261 (2014).
25. Bolshan, Y. et al. Synthesis, optimization, and evaluation of novel small molecules as antagonists of WDR5-MLL interaction. *ACS Med. Chem. Lett.* **4**, 353–357 (2013).
26. Siladi, A. J. et al. WIN site inhibition disrupts a subset of WDR5 function. *Sci. Rep.* **12**, 1848 (2022).
27. Thomas, L. R. et al. Interaction of the oncoprotein transcription factor MYC with its chromatin cofactor WDR5 is essential for tumor maintenance. *Proc. Natl Acad. Sci. USA* **116**, 25260–25268 (2019).
28. Teuscher, K. B. et al. Discovery of potent orally bioavailable WD repeat domain 5 (WDR5) inhibitors using a pharmacophore-based optimization. *J. Med. Chem.* **65**, 6287–6312 (2022).
29. Zhu, J. et al. Gain-of-function p53 mutants co-opt chromatin pathways to drive cancer growth. *Nature* **525**, 206–211 (2015).
30. Sun, Y. et al. WDR5 supports an N-Myc transcriptional complex that drives a protumorigenic gene expression signature in neuroblastoma. *Cancer Res.* **75**, 5143–5154 (2015).
31. Getlik, M. et al. Structure-based optimization of a small molecule antagonist of the interaction between WD repeat-containing protein 5 (WDR5) and mixed-lineage leukemia 1 (MLL1). *J. Med. Chem.* **59**, 2478–2496 (2016).
32. Dolle, A. et al. Design, synthesis, and evaluation of WD-repeat-containing protein 5 (WDR5) degraders. *J. Med. Chem.* **64**, 10682–10710 (2021).
33. Yu, X. et al. A selective WDR5 degrader inhibits acute myeloid leukemia in patient-derived mouse models. *Sci. Transl. Med.* **13**, eabj1578 (2021).
34. Yu, X. et al. Discovery of potent and selective WDR5 proteolysis targeting chimeras as potential therapeutics for pancreatic cancer. *J. Med. Chem.* **66**, 16168–16186 (2023).

35. Niesen, F. H., Berglund, H. & Vedadi, M. The use of differential scanning fluorimetry to detect ligand interactions that promote protein stability. *Nat. Protoc.* **2**, 2212–2221 (2007).

36. Senisterra, G., Chau, I. & Vedadi, M. Thermal denaturation assays in chemical biology. *Assay. Drug Dev. Technol.* **10**, 128–136 (2012).

37. Schuetz, A. et al. Structural basis for molecular recognition and presentation of histone H3 by WDR5. *EMBO J.* **25**, 4245–4252 (2006).

38. Krissinel, E. & Henrick, K. Inference of macromolecular assemblies from crystalline state. *J. Mol. Biol.* **372**, 774–797 (2007).

39. Gurung, R., Om, D., Pun, R., Hyun, S. & Shin, D. Recent progress in modulation of WD40-repeat domain 5 protein (WDR5): inhibitors and degraders. *Cancers* **15**, 3910 (2023).

40. Li, D. et al. Discovery of a dual WDR5 and Ikaros PROTAC degrader as an anti-cancer therapeutic. *Oncogene* **41**, 3328–3340 (2022).

41. Schwalm, M. P. et al. Tracking the PROTAC degradation pathway in living cells highlights the importance of ternary complex measurement for PROTAC optimization. *Cell Chem. Biol.* **30**, 753–765 e8 (2023).

42. Wang, R. et al. Selective targeting of non-centrosomal AURKA functions through use of a targeted protein degradation tool. *Commun. Biol.* **4**, 640 (2021).

43. Chen, C. R. & Makhatadze, G. I. ProteinVolume: calculating molecular van der Waals and void volumes in proteins. *BMC Bioinforma.* **16**, 101 (2015).

44. Hutchinson, A. & Seitova, A. Production of recombinant PRMT proteins using the baculovirus expression vector system. *J. Vis. Exp.* **173**, e62510 (2021).

45. Burgess-Brown, N. A. et al. Screening and production of recombinant human proteins: protein production in E. coli. *Methods Mol. Biol.* **2199**, 45–66 (2021).

46. Kabsch, W. Integration, scaling, space-group assignment and post-refinement. *Acta Crystallogr. D. Biol. Crystallogr.* **66**, 133–144 (2010).

47. Afonine, P. V. et al. Towards automated crystallographic structure refinement with phenix.refine. *Acta Crystallogr. D. Biol. Crystallogr.* **68**, 352–367 (2012).

48. Emsley, P. & Cowtan, K. Coot: model-building tools for molecular graphics. *Acta Crystallogr. D. Biol. Crystallogr.* **60**, 2126–2132 (2004).

Acknowledgements

Author contributions

M.F.M.: investigation, visualization, data curation, formal analysis, validation, crystal structure solving of all PROTAC complexes, writing the original manuscript draft, writing—review & editing., B.W.: investigation, formal analysis, validation, writing the original manuscript draft, writing —review & editing., M.N.: investigation, visualization, validation, writing —review & editing., S.W.K.: investigation, validation, writing—review & editing., A.M.: investigation, validation, formal analysis, writing—review & editing., C.K.: investigation., H.G.Á.: investigation, writing—review & editing., S.S.: investigation., M.M.: investigation, writing—review & editing., L. Hoffer: formal analysis, validation, writing—review & editing., M.C.: investigation, validation, and writing—review & editing., J.A.: investigation., A.S.L.: investigation, writing—review & editing., T.H.: investigation, writing—review & editing., S.T.: investigation, writing—review & editing., S.G.: investigation, M.S.: investigation., D.B.L.: investigation., V.S.: resources., S.A.: resources., P.L.: investigation., Y.L.: investigation, A.S.: investigation, T.K.: investigation, J.G.W.: investigation, G.G.P.: resources., D.A.K.: resources., B.P.: investigation., V.R.: investigation., A.V.: investigation, supervising, validation, writing—review & editing., B.R.: investigation, supervising, validation, analytical data review, writing—review & editing, A.A.: Supervision, G.P.: supervision, formal analysis, validation, writing—review & editing., D.U.: supervision, formal analysis, writing—review & editing., J.R.: supervision, formal analysis, writing—review & editing. L. Halabelian: supervision, validation, writing—review & editing. R.M.: supervision, formal analysis, writing—review & editing. R.A.: conceptualization, supervision, formal analysis, writing—review & editing, fund acquisition. M.V.: conceptualization, supervision, formal analysis, writing the original manuscript draft, writing—review & editing the manuscript, Fund acquisition.

Competing interests

The authors declare no competing interests.

Additional information

Supplementary information The online version contains supplementary material available at https://doi.org/10.1038/s41467-024-54500-x.

Correspondence and requests for materials should be addressed to Rima Al-awar or Masoud Vedadi.

Peer review information *Nature Communications* thanks Gang Greg Wang and the other anonymous reviewer(s) for their contribution to the peer review of this work. A peer review file is available.

Reprints and permissions information is available at http://www.nature.com/reprints

Publisher's note Springer Nature remains neutral with regard to jurisdictional claims in published maps and institutional affiliations.